Journal of Computational Physics 501 (2024) 112798

Contents lists available at ScienceDirect

Journal of Computational Physics

journal homepage: www.elsevier.com/locate/jcp

A scalable well-balanced numerical scheme for the modeling of two-phase shallow granular landslide consolidation

Federico Gatti [a,b,c,*], Carlo de Falco [b], Simona Perotto [b], Luca Formaggia [b], Manuel Pastor [c]

[a] *Consiglio Nazionale delle Ricerche - Istituto di Matematica Applicata e Tecnologie Informatiche "E. Magenes" (CNR-IMATI), Via Ferrata 1, 27100, Pavia, Italy*

[b] *MOX – Modelling and Scientific Computing, Department of Mathematics Politecnico di Milano, Piazza Leonardo da Vinci 32, 20133 Milano, Italy*

[c] *Department of Applied Mathematics, ETS Ingenieros de Caminos, Universidad Politécnica de Madrid, Calle del Profesor Aranguren, 3, 28040 Madrid, Spain*

ARTICLE INFO

Keywords:
Taylor-Galerkin scheme
Path-conservative methods
Quadtree mesh
Parallel simulations
Two-phase model
Debris flow

ABSTRACT

We introduce a new method to efficiently solve a variant of the Pitman-Le two-phase depth-integrated system of equations, for the simulation of a fast landslide consolidation process. In particular, in order to cope with the loss of hyperbolicity typical of this system, we generalize Pelanti's proposition for the Pitman-Le model to the case of a non-null excess pore water pressure configuration. The variant of the Pitman-Le model is numerically solved by relying on the approach the authors set to discretize the corresponding single-phase model, jointly with a fictitious inter-phase drag force which avoids arising the spurious numerical oscillations induced by the loss of hyperbolicity. To verify the reliability of the proposed simulation tool, we first assess the accuracy and efficiency of the new method in ideal scenarios. In particular, we investigate the well-balancing property and provide some relevant scaling results for the parallel implementation of the method. Successively, we challenge the procedure on real configurations from the available literature.

1. Introduction

In the field of landslide propagation forecasting, a number of continuum mathematical models have been developed during the years. While the comparison of the horizontal propagation length scale of the landslide with the vertical one suggests the use of depth-integrated models, the different behavior of various types of landslide, such as debris flows and mudflows, entails the need to define more detailed mathematical models. Among the simplest ones in the literature, single-phase viscous models consider the landslide as a single material having proper mechanical and rheological properties. These models can be used for the description of mudflows since they consist of roughly homogeneous mixtures of fine soil particles and water. Even if single-phase models can provide accurate results for such types of land movement, they do not represent a viable option for the description of debris flows propagation, since solid particles and water content can have considerably different velocities. In fact, a reliable mathematical model for debris flows

* Corresponding author at: Consiglio Nazionale delle Ricerche - Istituto di Matematica Applicata e Tecnologie Informatiche "E. Magenes" (CNR-IMATI), Via Ferrata 1, 27100 Pavia, Italy.

E-mail addresses: federico.gatti@imati.cnr.it (F. Gatti), carlo.defalco@polimi.it (C. de Falco), simona.perotto@polimi.it (S. Perotto), luca.formaggia@polimi.it (L. Formaggia), manuel.pastor@upm.es (M. Pastor).

https://doi.org/10.1016/j.jcp.2024.112798
Received 4 August 2023; Received in revised form 20 November 2023; Accepted 22 January 2024

Available online 24 January 2024

should include the velocities of both solid and liquid phases as well as the internal stresses. Among the most notable contributions in this direction, we mention the works by E.B. Pitman and L. Le [1] and by S.P. Pudasaini [2]. More recently, M. Pastor and co-workers developed a mathematical model which somehow generalizes the Pitman-Le and the Pudasaini set of equations, see [3,4]. This generalized model takes into account the importance of the pore pressure, by adding a three-dimensional consolidation equation tracking the evolution of the excess pore water pressure inside the landslide to the mass and momentum balance laws. The effective role that pore water pressure plays is corroborated by practical experience. For instance, a possible mitigation strategy to slow down the landslide velocity comes from the use of basal grids where the pore pressure is made zero (see [5–7]). Furthermore, the two-phase consolidation model in [3,4] is consistent with the Pitman-Le set of equations when null excess pore water pressure is considered.

Several numerical methods have been developed to approximate both the single- and the two-phase landslide models. Among them, the TG2-PC method [8] has been employed for the approximation of the single-phase model, reaching good results in terms of parallel efficiency and accuracy. The TG2-PC scheme is able to combine the flexibility, robustness, ease of implementation and parallel efficiency characterizing the TG2 scheme [9–11] with the capability of the Path-Conservative (PC) strategy to deal with nonconservative products. Indeed, the PC method has been successfully used in the literature in combination with finite-volume (FV) and discontinuous Galerkin (DG) approximations [12–17] and proved to provide a well-balanced discretization of the shallow-water equations, provided that an appropriate path is chosen (see [18]). Nevertheless, we mention the notable contributions to the approximation of the Pitman-Le equations with FV and DG schemes in combination with PC method in [19,20]. Furthermore, while the PC method offers an elegant way to construct well-balanced numerical schemes, other choices are possible. For instance, in [21,22], staggered semi-implicit hybrid FV/continuous finite-element schemes proved to be very effective in modeling the shallow water equations, by providing reliable results while relieving from severe restrictions on the time step selection. Concerning the approximation of Pastor's extension of the Pitman-Le model, we mention the Smooth Particle Hydrodynamics (SPH) model developed in [23–26]. SPH model provides valuable results in terms of accuracy and capability to deal with large material deformations. However, it shows some limitations related to parallel efficiency and treatment of discontinuities in the input topography (i.e., the bed of the landslide). Indeed, in the presence of a non-smooth topography, the computation of the corresponding gradient may lack meaning. This requires a pre-processing of the input topography before serving it as an input to the SPH model in order to avoid possible instabilities. It is then clear that studies that imply the presence of urban areas where the presence of houses provides discontinuities in the topography profile become problematic for schemes such as the SPH model (we refer, e.g., to [27–29] for examples in the case of flood problems).

In this work, we propose a scalable numerical scheme for the solution of Pastor's two-phase consolidation model by the TG2-PC scheme. The numerical scheme is implemented in a parallel MPI framework, where the domain discretization is performed with hierarchical quadtree meshes, following [11]. Furthermore, thanks to the PC formulation in a continuous finite element framework, the method allows dealing with arbitrary geometries, thus avoiding issues related to the direct computation of the gradient of the topography. When compared with the single-phase paradigm, the two-phase consolidation model suffers some drawbacks, such as the lack of an explicit expression for the eigenvalues of the corresponding quasilinear system and the loss of hyperbolicity, which leads to the rise of numerical oscillations. For this reason, we propose an extension to Pelanti's proposition related to the eigenstructure of the Pitman-Le equations to the case where the excess pore water pressure cannot be neglected.

The paper is organized as follows. In Section 2 we describe the model equations. In Section 3 we introduce the proposed numerical scheme, while in Section 4 we perform numerical tests. Here, we first show results on ideal scenarios targeting both accuracy and parallel efficiency, then we consider a real case study to show that the method can be effectively used in real applications. Finally, in Section 5 we draw some conclusions and discuss some future developments.

2. Shallow two-phase consolidation equations

Consider a Cartesian domain $\Omega = (0, L_x) \times (0, L_y) \subset \mathbb{R}^2$ characterized by a subdomain $\Omega_w(t) \subset \Omega$ which identifies the region of landslide material, whose extension varies in space and time. Region $\Omega_w(t)$ is defined as the portion of Ω where the total depth, h, of the mixture and the landslide height, h_w, h_s, of the fluid and solid phases are positive. In particular, we assume $\Omega_w(t) \subset \Omega$ during the whole simulation time window, namely for $t \in (0, T]$, being T the final time.

According to [3], the balance equations for mass and momentum consist of the set of coupled nonlinear depth-integrated partial differential equations in $\Omega_w \times (0, T]$,

$$\begin{cases} \partial_t h_\alpha + \nabla \cdot \mathbf{U}_\alpha = n_\alpha e_R, \\ \partial_t \mathbf{U}_\alpha + \nabla \cdot \left(\mathbf{U}_\alpha \otimes \mathbf{v}_\alpha + \overline{P}_\alpha h \mathbb{I} \right) - \left(\frac{1}{2} \frac{\rho_w}{\rho_\alpha} g h^2 + \frac{h \overline{\Delta p}}{\rho_\alpha} \right) \nabla n_\alpha + g h_\alpha \nabla Z = \frac{1}{\rho_\alpha} \mathbf{S}_\alpha, \end{cases} \tag{1}$$

supplemented by suitable initial and boundary conditions, where the sub-index $\alpha = w, s$ denotes the fluid (w) or solid (s) phase. Here, h_α is the phase height; $\mathbf{U}_\alpha$ denotes the phase mass flux; n_α is the phase porosity, with $n_w + n_s = 1$; e_R is the erosion rate; $\mathbf{v}_\alpha = (v_{\alpha,x}, v_{\alpha,y})^T = \mathbf{U}_\alpha / h_\alpha$ denotes the phase velocity; $\overline{P}_\alpha$ represents the depth-averaged phase pressure per unit density; $\mathbb{I}$ is the identity tensor; ρ_α is the phase density; g is the gravitational acceleration; $\overline{\Delta p}$ denotes the depth-averaged excess pore water pressure (pwp); Z is the topography profile; $\mathbf{S}_\alpha$ indicates the source term.

Concerning the state variables, it turns out that $h_\alpha = h n_\alpha$, $\mathbf{U}_\alpha = (U_{\alpha,x}, U_{\alpha,y})^T$, $\mathbf{U} = \mathbf{U}_w + \mathbf{U}_s$, with $\mathbf{U}$ the mixture mass flux, so that, the mixture velocity is defined by $\mathbf{v} = (v_x, v_y)^T = \mathbf{U}/h = n_s \mathbf{v}_s + n_w \mathbf{v}_w$; the depth-averaged phase pressures

$$\overline{P}_w = \frac{1}{2} g h_w + n_w \frac{\overline{\Delta p}}{\rho_w}, \quad \overline{P}_s = \frac{1}{2} g h_s - n_w \frac{\overline{\Delta p}}{\rho_s} \tag{2}$$

consist of two contributions, i.e., i) a hydrostatic term, which varies linearly vertically according to the classical hydrostatic law [30], and ii) a term depending on the excess pwp, that has to be computed from the consolidation equation (see below for more details); the erosion rate is modeled by the Hungr's law [31], so that the total volume of material height increases according to a specific rate, namely

$$e_R = E_s |\mathbf{U}|, \tag{3}$$

with E_s the entrainment coefficient computed starting from the initial and the final material volume and the traveled distance; the source term $\mathbf{S}_\alpha$ includes the contribution of the basal shear stress ($\boldsymbol{\tau}_B^{(\alpha)}$) and the interaction between solid and liquid phases ($\mathbf{R}^{(\alpha)}$), being $\mathbf{S}_\alpha = \boldsymbol{\tau}_B^{(\alpha)} + \mathbf{R}^{(\alpha)} h$. In particular, concerning $\boldsymbol{\tau}_B^{(\alpha)} = (\tau_{B,x}^{(\alpha)}, \tau_{B,y}^{(\alpha)})^T$, we do not consider any bed friction contribution for the fluid (i.e., we set $\boldsymbol{\tau}_B^{(w)} = \mathbf{0}$), and we adopt the Voellmy's rheological law for the solid phase, namely we define

$$\tau_{B,i}^{(s)} = -\left[\left(\rho_d' g h - \Delta p^b \right) \frac{1}{|v_i|} \tan(\phi_B) + \rho g \frac{|v_i|}{\xi} \right] v_i \quad \text{for} \quad i = x, y, \tag{4}$$

with $\rho_d' = n_s(\rho_s - \rho_w)$ the effective density, Δp^b the bed excess pwp, ϕ_B the basal friction angle, $\rho = n_s \rho_s + n_w \rho_w$ the mixture density and ξ the turbulence coefficient. The Voellmy's rheology is composed by two contributions, the first one derives from the Coulomb friction term [32] that vanishes in a fully liquefied state (i.e., $\Delta p^b = \rho_d' g h$), the second contribution represents the energy loss due to the turbulence stress [33–35]. As far as the solid-liquid interaction is concerned, we set $\mathbf{R}^{(w)} = -\mathbf{R}, \mathbf{R}^{(s)} = \mathbf{R}$ with

$$\mathbf{R} = C_d (\mathbf{v}_w - \mathbf{v}_s), \tag{5}$$

the interphase drag, where C_d is the friction coefficient, modeled through the Anderson and Jackson law [36], as

$$C_d = \frac{n_w n_s}{V_T n_w^m} \left(\rho_s - \rho_w \right) g, \tag{6}$$

with V_T the terminal velocity and m an integer taking the value 1 or 2 according to the flow condition [36] (in the sequel, we take $m = 1$ if not otherwise stated). For further details on the source term, we refer to [3,37,38].

Following [39,3,4], we complete model (1) with the three-dimensional consolidation equation

$$\frac{D_z \Delta p}{Dt} + \mathbf{v}_s \cdot \nabla \Delta p - C_v \partial_{zz} \Delta p = \rho_d' g (1 - \zeta) e_R - C_1 (\mathbf{v}_w - \mathbf{v}_s) \cdot \nabla h_w - C_1 h_w \nabla \cdot \mathbf{v}_w - C_2 h_s \nabla \cdot \mathbf{v}_s, \tag{7}$$

to be solved in $\Omega_w \times (0, h) \times (0, T]$, with $\zeta = z/h$ and where

$$\frac{D_z}{Dt} = \partial_t + a_z \partial_z \quad \text{with} \quad a_z = e_R (1 - \zeta), \tag{8}$$

denotes the material derivative associated with the vertically moving domain, with a_z the relative vertical velocity with respect to a domain that moves at velocity $e_R \zeta$ (we refer to [4] for a derivation of (7)), Δp is the three-dimensional excess pwp, C_v is the consolidation coefficient, C_1 and C_2 are defined by

$$C_1 = \rho_d' g (1 - \zeta) - \frac{E_m}{h}, \quad C_2 = \rho_d' g (1 - \zeta) + \frac{E_m}{n_s} \frac{n_w}{h}, \tag{9}$$

with E_m the odometric modulus. Note that $\Delta p = \Delta p(x, y, z, t)$ is linked to $\overline{\Delta p}$ in (1) through the depth-integration, namely

$$\overline{\Delta p} = \frac{1}{h} \int_0^h \Delta p \, dz, \tag{10}$$

while Δp^b in (4) coincides with the evaluation of the excess pwp at the bottom surface (i.e., $\Delta p^b = \Delta p(x, y, 0, t)$).

The presence of a diffusive contribution in (7) requires setting boundary conditions at both the endpoints of the vertical domain $(0, h)$. At the free surface we assume a null excess pwp since subject to the atmospheric pressure, while at the bottom we prescribe a basal excess pwp or we consider a zero boundary flux in case the material is flowing over an impermeable layer. In addition, a suitable initial condition has to be added to equation (7) as the consolidation problem is very sensitive to such a data. In this work, we assume that a region close to the bottom develops an excess pwp close to the liquefaction value $\rho_d' g h$.

As proved in [3], system (1) is completely consistent with the classical Pitman-Le set of equations in the case of null excess pwp. The eigenstructure of the quasilinear form of the Pitman-Le equations has been widely studied in the literature [1,40–42]. In particular, we propose here the generalization of an important result proved by M. Pelanti and collaborators in [40] to equations (1), namely to the case of the Pitman-Le model with a non-null excess pwp. To this aim, we focus on a one-dimensional setting, so that v_w, v_s denote the phase velocity components for the liquid and solid parts, respectively.

Proposition 2.1. *The Jacobian matrix associated with the transport operators in (1) has always at least two real eigenvalues, λ_1, λ_4, named external eigenvalues and two internal eigenvalues, λ_2, λ_3, that can be complex, satisfying the inequalities,*

$$v_{\min} - c_1 \le \lambda_1 \le \mathcal{R}(\lambda_2) \le \mathcal{R}(\lambda_3) \le \lambda_4 \le v_{\max} + c_1, \tag{11}$$

where $\mathcal{R}(\cdot)$ denotes the real part, $v_{\min} = \min(v_w, v_s)$, $v_{\max} = \max(v_w, v_s)$, $c_1 = \dfrac{1}{2\sqrt{\rho_w}}\sqrt{B + \sqrt{C}}$, with

$$\begin{aligned} B &= 4\beta^2\overline{\Delta p} + 2a^2\rho_w(1+\beta^2), \\ C &= B^2 - 16a^2\beta^2\rho_w^2\left(a^2 + \frac{\overline{\Delta p}}{\rho_w}\right), \end{aligned} \tag{12}$$

being $\beta = \sqrt{\dfrac{1}{2}n_w(1-r)}$, with $r = \rho_w/\rho_s$, and $a = \sqrt{gh}$. Furthermore, if $n_w \neq 0$, a sufficient condition to guarantee the strict hyperbolicity of system (1) is

$$|v_s - v_w| \le 2c_2 \quad \text{or} \quad |v_s - v_w| \ge 2c_1, \tag{13}$$

for the velocity, with $c_2 = \dfrac{1}{2\sqrt{\rho_w}}\sqrt{B - \sqrt{C}}$, and

$$-\rho_w a^2 \le \overline{\Delta p} \le \rho_w a^2 \frac{1+r}{2}\frac{h_s}{h_w}, \tag{14}$$

for the mean excess pwp.

The proof of this result can be found in Appendix A. In [40], for the Pitman-Le equations, the authors use the Newton method to recover the full wave structure during the evolution of the simulation in order to exploit the approximate Riemann-Roe solver. Here, for the two-phase consolidation model, we rely on the fast Rusanov flux which is a single wave solver and requires just an estimation of the maximum simple wave speed in modulus.

Finally, we observe that the two-phase consolidation system of equations (1) and (7) admits a steady state solution which is similar to the 'lake at rest' configuration typical of the single-phase model, namely

$$h + Z = \text{constant}, \quad \mathbf{U}_\alpha = \mathbf{0}, \quad n_\alpha = \text{constant}, \quad \overline{\Delta p} = 0. \tag{15}$$

We refer to (15) as the well-balancing condition (or C-property). For the shallow water system, extensive research has been dedicated to design numerical methods consistent with (15) (see, e.g., [43–49,12,18,50]). We will numerically verify that the numerical scheme proposed in the next section satisfies the condition (15). Proposition 2.1 will play a crucial role in the setting and analysis of such an approach.

3. Numerical scheme

As a first step, we introduce the fully conservative wet-dry numerical strategy we adopt. We propose the two-phase extension of the procedure in [9,10,51] that has been successfully applied to the one-phase model in [11,8,22].
To this aim, we set the numerical thresholds, $h_{s,\min}$, $h_{w,\min}$, for the height of the solid and liquid, respectively. Below these values, we set null transport fluxes, and we neglect the bed friction contributions in order to avoid numerical instabilities in close to dry regions. Thus, the mass and momentum equations in (1) reduce to

$$\begin{cases} \partial_t h_\alpha = 0, \\ \mathbf{U}_\alpha = \mathbf{0} \end{cases} \tag{16}$$

in dry regions, that is, for $h_\alpha < h_{\alpha,\min}$.

Moreover, to define the solid/liquid porosity, we set another threshold, $h_{\min}$, on the material height below which we assign null porosity. Furthermore, below the threshold $h_{\min}$, we assume null excess pwp and do not solve the consolidation equation. This expedient turns out to be particularly useful since it allows us to write the model (1) and (7) in the entire computational domain Ω rather than in the wet region Ω_w only.

3.1. Discretization of the mass and of the momentum equations

We rewrite equation (1) as a balance law with a non-conservative term, namely as

$$\partial_t \mathbf{q} + \nabla \cdot \mathbf{F} + \mathbf{B}\nabla\mathbf{q} = \mathbf{S} \quad \text{in } \Omega \times (0, T]. \tag{17}$$

In particular, the vector of conserved variables is

$$\mathbf{q} = \begin{bmatrix} h_w \\ h_s \\ \mathbf{U}_w \\ \mathbf{U}_s \\ Z \end{bmatrix}; \tag{18}$$

the tensor $\mathbf{F}$ of transport fluxes is defined by

$$\mathbf{F}(\mathbf{q}, \overline{\Delta p}, \theta) = \begin{bmatrix} U_{w,x} & U_{w,y} \\ U_{s,x} & U_{s,y} \\ \frac{U_{w,x}^2}{h_w} + \frac{1}{2} g h_w^2 + (1-\theta)\frac{h_w \overline{\Delta p}}{\rho_w} & \frac{U_{w,x} U_{w,y}}{h_w} \\ \frac{U_{w,x} U_{w,y}}{h_w} & \frac{U_{w,y}^2}{h_w} + \frac{1}{2} g h_w^2 + (1-\theta)\frac{h_w \overline{\Delta p}}{\rho_w} \\ \frac{U_{s,x}^2}{h_s} + \frac{1}{2} g h_s^2 + \frac{1}{2} g (1-r) h_s h_w - (1-\theta)\frac{h_w \overline{\Delta p}}{\rho_s} & \frac{U_{s,x} U_{s,y}}{h_s} \\ \frac{U_{s,x} U_{s,y}}{h_s} & \frac{U_{s,y}^2}{h_s} + \frac{1}{2} g h_s^2 + \frac{1}{2} g (1-r) h_s h_w - (1-\theta)\frac{h_w \overline{\Delta p}}{\rho_s} \\ 0 & 0 \end{bmatrix}, \tag{19}$$

with $\theta = 0, 1$ an integer; the non-conservative contribution is cast via the multidimensional tensor $\mathbf{B}$, such that $\mathbf{B}\nabla\mathbf{q} = \mathbf{B}_x \partial_x \mathbf{q} + \mathbf{B}_y \partial_y \mathbf{q}$ with

$$\mathbf{B}_x(\mathbf{q}, \overline{\Delta p}, \theta) = \begin{bmatrix} 0 & 0 & 0 & 0 & 0 & 0 & 0 \\ 0 & 0 & 0 & 0 & 0 & 0 & 0 \\ (\theta - n_s)\frac{\overline{\Delta p}}{\rho_w} & g h_w + n_w \frac{\overline{\Delta p}}{\rho_w} & 0 & 0 & 0 & 0 & g h_w \\ 0 & 0 & 0 & 0 & 0 & 0 & 0 \\ r g h_s - (\theta - n_s)\frac{\overline{\Delta p}}{\rho_s} & -n_w \frac{\overline{\Delta p}}{\rho_s} & 0 & 0 & 0 & 0 & g h_s \\ 0 & 0 & 0 & 0 & 0 & 0 & 0 \\ 0 & 0 & 0 & 0 & 0 & 0 & 0 \end{bmatrix},$$

$$\mathbf{B}_y(\mathbf{q}, \overline{\Delta p}, \theta) = \begin{bmatrix} 0 & 0 & 0 & 0 & 0 & 0 & 0 \\ 0 & 0 & 0 & 0 & 0 & 0 & 0 \\ 0 & 0 & 0 & 0 & 0 & 0 & 0 \\ (\theta - n_s)\frac{\overline{\Delta p}}{\rho_w} & g h_w + n_w \frac{\overline{\Delta p}}{\rho_w} & 0 & 0 & 0 & 0 & g h_w \\ 0 & 0 & 0 & 0 & 0 & 0 & 0 \\ r g h_s - (\theta - n_s)\frac{\overline{\Delta p}}{\rho_s} & -n_w \frac{\overline{\Delta p}}{\rho_s} & 0 & 0 & 0 & 0 & g h_s \\ 0 & 0 & 0 & 0 & 0 & 0 & 0 \end{bmatrix}; \tag{20}$$

the source term is

$$\mathbf{S}(\mathbf{q}, \nabla\overline{\Delta p}, \theta) = \begin{bmatrix} n_w e_R \\ n_s e_R \\ \frac{1}{\rho_w}\mathbf{S}_w - \theta\frac{h_w}{\rho_w}\nabla\overline{\Delta p} \\ \frac{1}{\rho_s}\mathbf{S}_s + \theta\frac{h_w}{\rho_s}\nabla\overline{\Delta p} \\ 0 \end{bmatrix}. \tag{21}$$

The numerical method we adapt to discretize the mass and the momentum equations consists of the second-order Taylor-Galerkin Path-Conservative (TG2-PC) scheme on quadtree adaptive meshes. The same approach has been used to solve the equations of the single-phase fast landslide model in [11,8].

The TG2-PC method is a two-step procedure that combines the Taylor-Galerkin (TG2) approach with a Path-Conservative (PC) finite-element integration scheme to compute the non-conservative product in (17).

The main novelty with respect to what done in [8], is represented by the presence of the source term. Following [52], we discretize in time $\mathbf{S}$ by resorting to the Additive RK.2.A.2 scheme, which coincides with an IMplicit EXplicit (IMEX) Additive Runge-Kutta (ARK) method [52]. This time integration scheme is A-stable and the associated stability region essentially coincides with the one characterizing the fully explicit RK scheme, thus implying no further restriction on the time step. Finally, to numerically deal with the non-linearities involved in $\mathbf{S}$, we employ a semi-implicit discretization of the source term, to get rid of the intrinsic coupling between the mass and momentum sources. In particular, we solve both $(1)_1$ and $(1)_2$ with a semi-implicit scheme, which decouples the mass and the momentum equation, while discretizing the excess pwp equation with an ad-hoc technique detailed in Section 3.2.

Let us introduce a quadtree partition $\mathcal{D}$ of the computational domain Ω. We associate with $\mathcal{D}$ two discrete spaces, the space $\mathbb{Q}_0$ of the discontinuous piecewise constant basis functions and the space $\tilde{\mathbb{Q}}_1$ of the continuous bilinear finite-element functions, whose basis consists of the linear combinations of standard piecewise bilinear polynomials defined on quadrilateral structured grids at a different resolution in order to avoid extra degrees of freedom (dofs) in correspondence with the hanging nodes (see, e.g., [11,53] for more details).

To apply the TG2-PC scheme to (17), we introduce the sets $\{\phi_j^{(0)}, j = 1, \dots, M\}$ and $\{\tilde{\phi}_i^{(1)}, i = 1, \dots, N\}$ of the basis functions associated with $\mathbb{Q}_0$ and $\tilde{\mathbb{Q}}_1$, respectively with M the number of quadrilateral elements and N the number of dofs in $\mathcal{D}$. Thus, the TG2-PC approximation of the balance law in (17) can be formulated for $n \geq 0$ as

$$\begin{aligned} &(\mathbf{Q}^{n+\frac{1}{2}}, \phi_j^{(0)}) = (\mathbf{Q}^n, \phi_j^{(0)}) - \frac{\Delta t}{2}(\nabla\cdot\mathbf{F}_0^n, \phi_j^{(0)}) - \frac{\Delta t}{2}(\mathbf{B}_0^n\nabla\mathbf{Q}^n, \phi_j^{(0)}) + \frac{\Delta t}{2}(\mathbf{S}_0^{n+\frac{1}{2}}, \phi_j^{(0)}), \\ &(\mathbf{Q}^{n+1}, \tilde{\phi}_i^{(1)}) = (\mathbf{Q}^n, \tilde{\phi}_i^{(1)}) + \Delta t(\mathbf{F}^{*,n+\frac{1}{2}}, \nabla\tilde{\phi}_i^{(1)}) - \Delta t(\mathbf{B}_1^{n+\frac{1}{2}}\nabla\mathbf{Q}^{n+\frac{1}{2}}, \tilde{\phi}_i^{(1)}) - \Delta t\int_{\partial\Omega}\mathbf{F}^{*,n+\frac{1}{2}}\,\mathbf{n}\,\tilde{\phi}_i^{(1)}\,d\Sigma + \frac{\Delta t}{2}(\mathbf{S}_1^n + \mathbf{S}_1^{n+1}, \tilde{\phi}_i^{(1)}), \end{aligned} \tag{22}$$

with Δt the time step, $(\cdot,\cdot)$ the $L^2(\Omega)$-scalar product, $\mathbf{n}$ the unit outward normal vector to the boundary $\partial\Omega$ of Ω. In particular, $\mathbf{Q}^{n+o}$ denotes the discrete counterpart in time of the conserved variable $\mathbf{q}$ evaluated at time $t^{n+o} = t^n + o\Delta t$, with $o = 0, \frac{1}{2}, 1$; accordingly, we define

$$\mathbf{B}_\theta^{n+o} = \mathbf{B}(\mathbf{Q}^{n+o}, \overline{\Delta P}^{n+o}, \theta), \quad \mathbf{F}_\theta^{n+o} = \mathbf{F}(\mathbf{Q}^{n+o}, \overline{\Delta P}^{n+\frac{1}{2}+o}, \theta),$$

with $\overline{\Delta P}^{n+o}$ the discrete temporal counterpart of the averaged excess pwp at time t^{n+o}, being $o = 0, \frac{1}{2}, 1$ and $\theta = 0, 1$, and $\mathbf{S}_\theta^{n+o} = \mathbf{S}(\mathbf{Q}^{*,n+o}, \overline{\Delta P}^{n+o}, \theta)$, where $\mathbf{Q}^{*,n+o}$ means that the source term is treated semi-implicitly in order to decouple the mass and momentum balance equations; the numerical flux is built following the flux correction limiting procedure (FCT), i.e., such that

$$\mathbf{F}^{*,n+\frac{1}{2}} = (\mathbf{F}_1^{n+\frac{1}{2}} - \delta\mathbf{F}^n) + \phi\delta\mathbf{F}^n, \tag{23}$$

with $\delta\mathbf{F}^n$ the anti-diffusive flux to be defined later, and ϕ the piecewise constant FCT coefficient defined according to the Zalesak's procedure [54–56], specifically by following the quadtree version in [11].

We observe that the depth-averaged excess pwp contribution in the transport fluxes has been treated semi-implicitly following [57,58]. Moreover, the boundary flux integrals are computed by imposing non-reflecting boundary conditions. Finally, we adopt a mass lumping technique to solve the equation $(22)_2$ [11,8]. We point out that, to guarantee numerical stability for various choices of the terminal velocity V_T that could be chosen considerably lower than 1, we replace the Cranck-Nicolson time integration in $(22)_2$ with an implicit Euler scheme to guarantee L-stability. This is done just for the integration of the inter-phase drag force. Other choices could be investigated to maintain a stable discretization in case $V_T \ll 1$ and at the same time a second-order approximation of the inter-phase drag force. In particular, we mention the second-order L-stable scheme named Additive RK.2.L.1 method and described in [52]. However, the latter scheme could require a more restrictive choice for the time step through the CFL condition as one can evince from the absolute stability of the semi-discrete problem described in [52].

As confirmed by Proposition 2.1, the interphase drag plays a crucial role in stabilizing the model equations, the loss of hyperbolicity being a function of the relative phase velocity $\mathbf{v}_w - \mathbf{v}_s$ [59,60]. Nevertheless, there are some flow conditions where the presence of the interphase drag force is not sufficient to prevent the appearance of unphysical numerical oscillations due to the rise

of complex eigenvalues. Following [59,60], to guarantee the hyperbolicity of system (1), we design an extra numerical interphase drag, which is added to the numerical model (22) through the following predictor-corrector strategy. We denote by $\mathbf{Q}_{\mathrm{p}}^{n+1}$ the output of the predictor step that we identify with the solution to the TG2-PC scheme (22). Then, the corrector step recovers the updated solution $\mathbf{Q}^{n+1}$ defined by

$$\mathbf{Q}^{n+1} = \mathbf{Q}_{\mathrm{p}}^{n+1} + \Delta t\, \mathbf{s}(\mathbf{Q}^{n+1}), \tag{24}$$

where vector $\mathbf{s}$ denotes the numerical interphase drag which, when referred to continuous variables, is defined by

$$\mathbf{s}(\mathbf{q}) = \begin{bmatrix} 0 \\ 0 \\ -Dh(\mathbf{v}_w - \mathbf{v}_s) \\ rDh(\mathbf{v}_w - \mathbf{v}_s) \\ 0 \end{bmatrix}, \tag{25}$$

with D the drag coefficient. The discrete counterpart of coefficient D denoted by D^{n+1} is constructed by exploiting the sufficient condition for strict hyperbolicity stated in Proposition 2.1. Such a condition leads to the inequalities

$$D^{n+1} \geq \max\left(0, \frac{\frac{|\Delta \mathbf{v}_{pw,s}^{n+1}|}{2c_2^{n+1}} - 1}{\Delta t\left(\frac{1}{n_w^{n+1}} + \frac{r}{n_s^{n+1}}\right)}\right), \quad D^{n+1} \leq \min\left(0, \frac{\frac{|\Delta \mathbf{v}_{pw,s}^{n+1}|}{2c_1^{n+1}} - 1}{\Delta t\left(\frac{1}{n_w^{n+1}} + \frac{r}{n_s^{n+1}}\right)}\right), \tag{26}$$

where $\Delta \mathbf{v}_{pw,s}^{n+1} = \mathbf{v}_{pw}^{n+1} - \mathbf{v}_{ps}^{n+1}$, with $\mathbf{v}_{pw}^{n+1}, \mathbf{v}_{ps}^{n+1}$ the predicted velocities, n_w^{n+1}, n_s^{n+1} the updated values of the porosity and c_1^{n+1}, c_2^{n+1} the updated values of the external and internal wave celerity, respectively with c_1 and c_2 defined as in Proposition 2.1. In particular, according to [60,59], the first condition in (26) keeps the momentum equations in the physical hyperbolic regime. On the contrary, the second condition is not relevant from a physical point of view, a negative inter-phase drag coefficient being not physical.

We note that the presence of non-conservative products in (17) does not add any further significant complication to the numerical setting developed for the single-phase problem. The main issue is the computation of these products at the second step of the TG2-PC method $(22)_2$ since the gradient is not defined on the space $\mathbb{Q}_0$. To overcome such a problem, we adopt the same approach used to deal with the slope contribution, i.e., the PC method, in particular the finite element version proposed in [8]. To this aim, we consider the linear path

$$\mathbf{\Psi} = \mathbf{\Psi}(\mathbf{W}_-^{n+\frac{1}{2}}, \mathbf{W}_+^{n+\frac{1}{2}}, s) = \mathbf{W}_-^{n+\frac{1}{2}} + s(\mathbf{W}_+^{n+\frac{1}{2}} - \mathbf{W}_-^{n+\frac{1}{2}}), \tag{27}$$

parametrized by the real parameter $s \in [0,1]$, which connects two adjacent states, $\mathbf{W}_-^{n+\frac{1}{2}} = (\mathbf{Q}_-^{n+\frac{1}{2}}, \overline{\Delta P}_-^{n+\frac{1}{2}})$, $\mathbf{W}_+^{n+\frac{1}{2}} = (\mathbf{Q}_+^{n+\frac{1}{2}}, \overline{\Delta P}_+^{n+\frac{1}{2}})$, associated with the mesh elements sharing the generic edge e, with barycenter located at $\mathbf{x}_-$ and $\mathbf{x}_+$, respectively. Then, the PC finite element formulation for the integral of the non-conservative products in $(22)_2$ is

$$(\mathbf{B}_1^{n+\frac{1}{2}} \nabla \mathbf{Q}^{n+\frac{1}{2}}, \tilde{\phi}_i^{(1)}) = \sum_{e \in \mathcal{E}_i} \left(\mathbf{Q}_+^{n+\frac{1}{2}} - \mathbf{Q}_-^{n+\frac{1}{2}}\right) \int_e \tilde{\phi}_i^{(1)} dl \int_0^1 \mathbf{B}_1\left(\mathbf{\Psi}(\mathbf{W}_-^{n+\frac{1}{2}}, \mathbf{W}_+^{n+\frac{1}{2}}, s)\right) \mathbf{n}_e \, ds, \tag{28}$$

where $\mathbf{B}_1\left(\mathbf{\Psi}(\mathbf{W}_-^{n+\frac{1}{2}}, \mathbf{W}_+^{n+\frac{1}{2}}, s)\right) = \mathbf{B}(\mathbf{Q}^{n+\frac{1}{2}}, \overline{\Delta P}^{n+\frac{1}{2}}, 1)$, $\mathcal{E}_i$ denotes the set of all the elements sharing the node i, $\mathbf{n}_e$ is the unit outward normal vector to the edge e, such that $\mathbf{n}_e \cdot (\mathbf{x}_+ - \mathbf{x}_-) > 0$. In practice, since the orientation of normal $\mathbf{n}_e$ can be along the x- or the y-direction only, the product in the last integral results in evaluating just the matrix $\mathbf{B}_x$ or $\mathbf{B}_y$ in (20) along the path $\mathbf{\Psi}$.
However, the absence of a diffusive flux in (17) requires a notable modification of the well-balanced Rusanov flux introduced in [8]. To this aim, following [61] and with reference to a single mesh element, say j, with extension Δx_j and Δy_j along the x- and y-direction, respectively, we propose the new well-balanced modification of the Rusanov numerical flux,

$$\delta \mathbf{F}_j^n = \min_{\left(\frac{\Delta x_j}{\Delta t}, \frac{\Delta y_j}{\Delta t}\right)} \frac{1}{2\Delta t} (\nabla \mathbf{V}^n, \phi_j^{(0)}), \tag{29}$$

where vector $\mathbf{V}^n$ is the time-discrete counterpart of the vector $\mathbf{v}$, which is linked to the vector $\mathbf{q}$ of the conserved variables through the relation $\mathbf{v} = \mathbf{U}\mathbf{q}$, with $\mathbf{U}$ the transformation matrix given by

$$\mathbf{U} = \begin{bmatrix} 1 & 0 & 0 & 0 & 0 & 0 & \gamma n_w u \\ 0 & 1 & 0 & 0 & 0 & 0 & \gamma n_s u \\ 0 & 0 & 1 & 0 & 0 & 0 & 0 \\ 0 & 0 & 0 & 1 & 0 & 0 & 0 \\ 0 & 0 & 0 & 0 & 1 & 0 & 0 \\ 0 & 0 & 0 & 0 & 0 & 1 & 0 \\ 0 & 0 & 0 & 0 & 0 & 0 & 0 \end{bmatrix}. \tag{30}$$

Here, $u = u(h - h_{\min})$ denotes the Heaviside step function, while the coefficient γ depends on the flow condition through the mixture Froude number Fr, being $\gamma = 1/(1 - \mathrm{Fr}^2)$. In the simulations of Section 4, we employ the maximum Froude number in the domain Ω at the given simulation time to compute the coefficient γ. Moreover, in the computation of the anti-diffusive Rusanov numerical flux (29), quantities $\Delta x_j/\Delta t, \Delta y_j/\Delta t$ are upper bounded, thanks to the CFL condition, by the maximum simple wave speed in both the directions that are estimated through Proposition 2.1.

Equation (29) offers a generalization of the well-balanced flux limiting procedure in [8], since the two formulas do coincide in the case of a low Froude number. In particular, when the coefficient γ is set equal to one, we recover the well-balanced Rusanov flux proposed in [8], by adding the fluid with the solid mass balance equations.

Finally, we underline that in the absence of a physical diffusive flux, the modification in (29) is essential to guarantee good stability conditions to the overall numerical scheme (22) in order to prevent the time step going to zero.

3.2. Discretization of the consolidation equation

To discretize equation (7), we propose a second order space-time scheme that combines the TG2-PC method, used to discretize the problem in the horizontal domain Ω, with a semi-Lagrangian finite difference scheme, adopted to approximate the vertical material derivative along the particle trajectory. However, in contrast to a standard semi-Lagrangian integration where the domain is fixed in time, the consolidation equation (7) considers a domain varying in time, since it follows the free surface dynamics that delimits the vertical domain extension. As a consequence, the vertical material derivative is discretized in a moving domain so that we will refer to such a discretization as to a Semi-Arbitrary-Lagrangian-Eulerian (SALE) scheme.

For any mesh node $z \in [0, h]$ along the vertical direction, we consider the non-dimensional coordinate $\zeta = z/h$, with $\zeta \in [0, 1]$ as defined in Section 2. Then, the characteristic curve $\zeta = \zeta(t)$ is the solution to the backward Cauchy problem

$$\begin{cases} \dfrac{d\zeta}{dt} = a_z(\mathbf{q}, \zeta(t)) \quad \text{in } [t^n, t^{n+o}), \\ \zeta(t^{n+o}) = \tilde{\zeta}, \end{cases} \tag{31}$$

with $o = \frac{1}{2}, 1$, $a_z = a_z(\mathbf{q}, \zeta(t))$ the vertical relative velocity defined as in (8), and $\tilde{\zeta}$ represents the final condition. According to [62,63], to preserve the second order accuracy of the space-time scheme, we integrate problem (31) with the explicit second order midpoint rule, namely we compute

$$\begin{aligned} &\zeta_0 = \tilde{\zeta}, \\ &\zeta_1 = \zeta_0 - \frac{\Delta t}{2} A_z^n(\zeta_0), \\ &\zeta_2 = \zeta_0 - \Delta t A_z^{n+\frac{1}{2}}(\zeta_1), \end{aligned} \tag{32}$$

where $A_z^n(\zeta)$ and $A_z^{n+\frac{1}{2}}(\zeta)$ denote the time discrete counterpart of a_z evaluated at $\mathbf{Q}^n$ and $\mathbf{Q}^{n+\frac{1}{2}}$, respectively at the generic vertical non-dimensional coordinate ζ.

We now introduce the operator $\mathcal{F}_\sigma^o$, with $\sigma = 0, 1, 2$ and $o = \frac{1}{2}, 1$, such that, when applied, e.g., to ΔP^n, denotes the evaluation of the quantity discrete in time ΔP^n at the vertical adimensional coordinate ζ_σ starting from the point $\tilde{\zeta} = \zeta(t^{n+o})$ and moving along the characteristic curve $\zeta = \zeta(t)$. Thus, by considering the same discrete spaces as in the previous section and denoting with S the right-hand side in (7), we can formulate the two-step second order horizontally discrete weak formulation, which leads us to look for $\Delta P^{n+1} = \Delta P^{n+1}(z)$ in $\tilde{\mathbb{Q}}_1$ such that

$$\begin{aligned} &(\Delta P^{n+\frac{1}{2}}, \phi_j^{(0)}) = (\mathcal{F}_1^{\frac{1}{2}}(\Delta P^n), \phi_j^{(0)}) - \frac{\Delta t}{2}(\mathbf{V}_s^n \cdot \nabla \mathcal{F}_1^{\frac{1}{2}}(\Delta P^n), \phi_j^{(0)}) + \frac{\Delta t}{2}(\mathcal{F}_1^{\frac{1}{2}}(S^n), \phi_j^{(0)}), \\ &(\Delta P^{n+1}, \tilde{\phi}_i^{(1)}) = (\mathcal{F}_2^1(\Delta P^n), \tilde{\phi}_i^{(1)}) - \Delta t(\mathbf{V}_s^{n+\frac{1}{2}} \cdot \nabla \mathcal{F}_1^1(\Delta P^{n+\frac{1}{2}}), \tilde{\phi}_i^{(1)}) + \Delta t(C_v \mathcal{F}_{\overline{m}}^1(\partial_{zz} \Delta P^m), \tilde{\phi}_i^{(1)}) + \Delta t(\mathcal{F}_1^1(S^{n+\frac{1}{2}}), \tilde{\phi}_i^{(1)}), \end{aligned} \tag{33}$$

with m and $\overline{m}$ integers to be properly defined, and $\mathbf{V}_s^{n+o}$ the time discrete solid velocity at time t^{n+o}. In particular, the horizontal transport contribution and the source terms are integrated with the variant of the PC method for a finite element discretization, analogously to as in (28). To recover the fully discrete formulation of the consolidation model, we employ the central finite difference scheme along the vertical direction. To this aim, we discretize the interval $[0, h]$ with 11 equally spaced nodes. Indices m and $\overline{m}$ in (33) are strictly related to the treatment (implicit or explicit) of the diffusive term, depending on the CFL condition at a given node of the mesh discretizing domain Ω. In more detail, we treat explicitly the diffusion term if the time step, Δt, needed to discretize the

mass and the momentum balance is lower than the time step required by the vertical diffusion contribution. In formulas, if $\Delta z_{n,i}$ is the mesh spacing along the vertical direction at time t^n and at the mesh node i, we have

$$m = \begin{cases} n \ \text{ if } \ \Delta t \leq \dfrac{\Delta z_{n,i}^2}{2C_v}(1-\mu^2) \\ n+1 \ \text{ otherwise,} \end{cases} \qquad \overline{m} = \begin{cases} 2 \ \text{ if } \ m = n, \\ 0 \ \text{ otherwise,} \end{cases} \tag{34}$$

with μ the CFL number related to the transport term of the consolidation equation. In Appendix B, we justify the derivation of the above time step restriction.

From a computational viewpoint, we observe that, in the case of an implicit scheme, we obtain a tridiagonal positive semi-definite linear system to be solved on the single mesh node of the computational domain Ω along the vertical direction. This does not affect the overall parallel implementation, since the independence among nodes i does not involve any communication among processors. Concerning the stability, the resulting scheme is stable under the same CFL condition required by the mass and momentum balance equations. Indeed, while the SALE method is unconditionally stable, the TG2-PC scheme in the horizontal plane Ω would require a CFL number μ due to the transport term that is always less restrictive than the CFL number needed to numerically stabilize equation (22). An additional advantage of this discretization relies on the treatment of the diffusion term. In close to dry regions $\Delta z_{n,i}$ could be fine enough to consider the case $m = n+1$ without modifying the order of accuracy with respect to the case $m = n$. This is a considerable advantage over a fully explicit scheme that would require the use of a smaller time step to prevent the rise of spurious oscillations.
Moreover, we point out that, as for the mass and the momentum equations, we apply a FCT procedure compliant with the one in the previous section to prevent the rise of numerical spurious oscillations in the horizontal discretization of the pressure equation with the TG2-PC.

Another advantage of the discretization in (33) is that the diffusion contribution does not appear in the first step of the method, in line with the TG2 method for advection dominated problems (see e.g. [9,11]). This choice does not affect the overall space-time second-order of accuracy of the method, under the hypothesis that the diffusion coefficient C_v is almost of the same order of magnitude of the time step ($C_v \sim \mathcal{O}(\Delta t)$). This requirement is, in general, verified in the case of a horizontally advection-dominated regime (we refer again to Appendix B).

Finally, we need to enforce the hyperbolicity behavior on the mean excess pwp as stated in Proposition 2.1. We note that the stabilization procedure adopted for the mass/momentum equation stabilization is similar to a penalty method (see, e.g., [64,65]). Thus, we again follow a predictor/corrector strategy first by defining the predicted vertically varying excess pwp, ΔP_p^{n+1}, through (33) and then by updating such a value with the corrector step

$$\Delta P^{n+1} = \Delta P_p^{n+1} - (\sigma_2 + \mathrm{sf}\sigma_1), \tag{35}$$

where sf is a safety factor set to 1.2 in numerical assessment, while σ_1, σ_2 are penalty parameters defined by

$$\sigma_1 = \min\left(\Delta P_p^{n+1} + \rho_w g h^{n+1}, 0\right), \tag{36}$$

$$\sigma_2 = \max\left(\Delta P_p^{n+1} - \rho_w g h^{n+1} \frac{1+r}{2} \frac{h_s^{n+1}}{h_w^{n+1}}, 0\right), \tag{37}$$

with ζ^{n+1} the numerical approximation of ζ at time t^{n+1}.
We mention that the integral means in the vertical direction are computed by means of the trapezoidal rule and that we consider a null vertical excess pwp profile for material height lower than the threshold $h_{\min}$.

4. Numerical examples

In this section, we focus on both benchmark and realistic configurations in order to verify the capability of the proposed numerical scheme to deal with academic problems as well as with real scenarios.

In all simulations, if not otherwise stated, the initial porosity is computed by exploiting the relation $n_w = (\rho - \rho_s)/(\rho_w - \rho_s)$ linking the mixture to the phase density. Regarding the thresholds under which we assign a null velocity, if not otherwise stated, we set $h_{w,\min} = 10^{-5}$ m, $h_{s,\min} = 10^{-5}$ m, $h_{\min} = 10^{-5}$ m. We keep the CFL condition equal to 0.9 in all the simulations. Furthermore, in the tests where we resort to a mesh adaptation procedure, we set a tolerance on the solution accuracy equal to 10^{-5} m.

4.1. Reliability tests

With a first set of simulations we aim to numerically investigate some properties of the proposed TG2-PC scheme when applied to the two-phase consolidation model. In more detail, we test the well-balance and the loss of hyperbolicity properties on reference configurations in the literature, we carry out the classical dam-break test case and we perform a parallel efficiency test.
For all the tests, except for the one adopted in the parallel efficiency analysis, we run the program with four MPI ranks available on a laptop with an Intel i7 CPU, a 2.60 GHz clock frequency and a 16 GB RAM. The efficiency analysis is executed in double precision on the supercomputer CINECA GALILEO100, where we perform the compilation and linking steps with gcc-10 and OpenMPI 4.1.1.

Table 1
Well-balancing tests. $L^\infty(\Omega)$-norm of the error for both the smooth and the discontinuous topography.

	$L^\infty(\Omega)$-norm of the error						
	h	n_w	$U_{w,x}$	$U_{w,y}$	$U_{s,x}$	$U_{s,y}$	$\overline{\Delta p}$
Z_1	1.77e-15	2.77e-17	8.01e-15	6.27e-15	2.40e-14	3.06e-14	5.99e-11
Z_2	6.66e-15	1.25e-15	3.84e-14	3.41e-14	4.07e-14	4.21e-14	5.57e-11

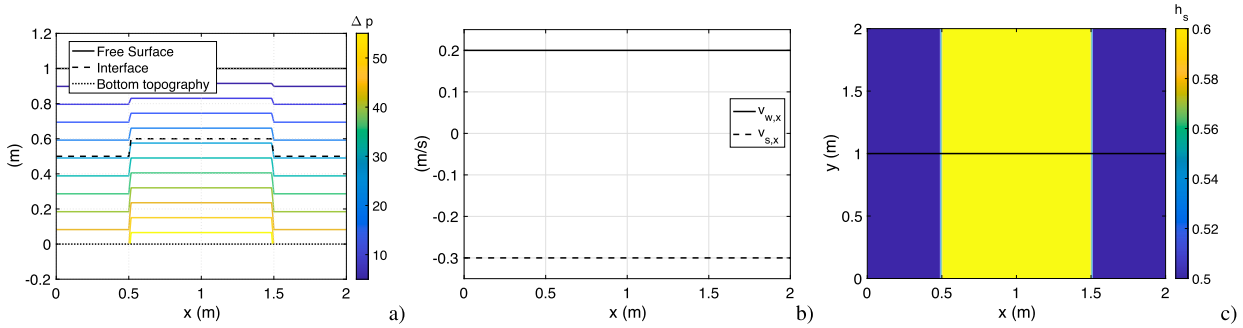

Fig. 1. Loss of hyperbolicity tests. Initial conditions for mass, momentum laws (panels a) and b)); colorplot of the solid/fluid interface (panel c)). (For interpretation of the colors in the figure(s), the reader is referred to the web version of this article.)

4.1.1. Well-balancing tests

To numerically verify the well-balancing property of the TG2-PC scheme, we analyze two examples with a smooth and a discontinuous topography, respectively. The tests are taken from [66] and have already been reproduced by the authors to investigate the well-balancing property of the same scheme in the case of the single-phase depth-integrated landslide model [8]. We consider a final time $T = 0.5$ s and a square domain with horizontal and vertical dimension $L_x = L_y = 10$ m; the smooth topography is described by

$$Z(\mathbf{x}) = Z_1(\mathbf{x}) = 5e^{-\frac{2}{5}(x-5)^2}, \tag{38}$$

while the discontinuous bottom is characterized by the function

$$Z(\mathbf{x}) = Z_2(\mathbf{x}) = \begin{cases} 4 & \text{if } 4 \le x \le 8, \\ 0 & \text{otherwise.} \end{cases} \tag{39}$$

Concerning the initial data, we assume a null initial excess pwp and phases at rest condition, with a total free surface height equal to 10 m and densities $\rho = 2350$ kg/m^3, $\rho_s = 2700$ kg/m^3, $\rho_w = 1000$ kg/m^3. The domain is discretized with a structured mesh consisting of 2^{14} elements.
Table 1 provides the $L^\infty(\Omega)$-norm of the error associated with the material height, the liquid porosity, the components of the liquid and solid mass fluxes and the mean excess pwp, for both the considered topographies. All the errors are close to the roundoff unit, independently of the selected bed profile. This confirms the well-balancing property of the proposed TG2-PC method for the two-phase consolidation model equations.

4.1.2. Loss of hyperbolicity tests

This test is proposed in [59] to assess the capability of the predictor/corrector strategy to recover the system hyperbolicity when applied to the two-layer shallow water system. The same configuration has been also considered to test the performance of the Non-Oscillatory Central (NOC) scheme when solving the Pitman-Le set of equations [60].
In the following we consider two tests, without and with excess pwp. In particular, in the latter case, we set an initial excess pwp profile which varies linearly from a liquefied value at the bottom to a null excess pwp at the free surface. We do not consider any roughness or erosion in the mass and momentum balance law. We set a final time $T = 1$ s, and consider a domain with an extension along the x- and y-direction equal to $L_x = L_y = 2$ m, respectively. The domain is discretized with a structured mesh consisting of 2^{14} cells, corresponding to a resolution along the x-direction of roughly $\Delta x \approx 0.01$ m. We set $r = 0.99$. Finally, the initial condition for the mass and the momentum equations coincides with

$$\mathbf{q}(\mathbf{x}, 0) = \begin{cases} (0.4, 0.6, 0.08, 0, -0.18, 0, 0)^T & \text{if } 0.5 < x < 1.5, \\ (0.5, 0.5, 0.10, 0, -0.15, 0, 0)^T & \text{otherwise.} \end{cases} \tag{40}$$

Fig. 1 graphically represents the initial conditions. In particular, panel a) shows the isolines associated with Δp together with the profile of the free surface, the solid/fluid interface, and the bottom topography. Panel b) shows the phase velocities. Panel c) provides the colorplot of the solid/fluid interface, while the black line identifies the section along which we analyze the solution trend.

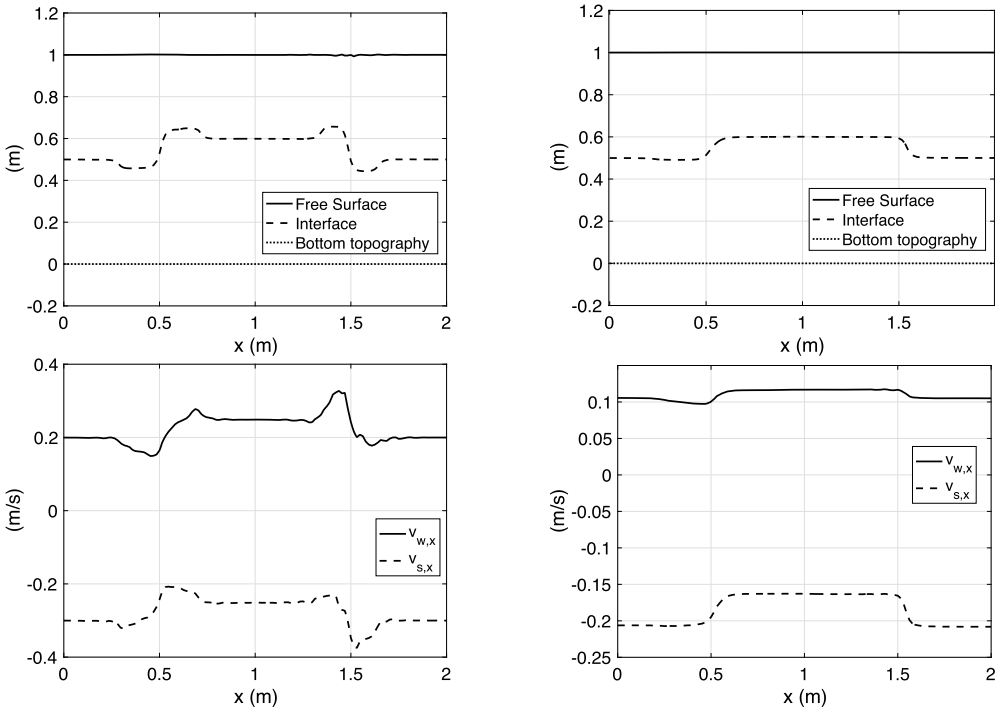

Fig. 2. Loss of hyperbolicity tests (null excess pwp). Trend of the free surface and of the phase interface evolution (top), and of the phase velocities (bottom) at the final time T provided by the TG2-PC scheme without (left) and with (right) the predictor/corrector step.

In a first analysis, we neglect the excess pwp equation so that we recover the Pitman-Le system of equations. In particular, for $r \approx 1$, the behavior of the Pitman-Le system is similar to the one of the two-layer shallow water equations according to [59]. Note that the initial data in (40) does not fit with the hyperbolic regime. Indeed, referring to Proposition 2.1, we recover the Pelanti's conditions

$$\begin{aligned} &|v_{w,x} - v_{s,x}| = 0.5 < 2\sqrt{gh} \approx 6.26, \\ &|v_{w,x} - v_{s,x}| = 0.5 > 2\sqrt{gh}\sqrt{\frac{1}{2}n_w(1-r)} \approx \begin{cases} 0.28 & \text{if } n_w = 0.4 \\ 0.31 & \text{otherwise,} \end{cases} \end{aligned} \tag{41}$$

for the case of null excess pwp. The system looses hyperbolicity at the beginning of the simulation at each point of the domain, since $2a\beta < |v_{w,x} - v_{s,x}| < 2a$.

Fig. 2 shows the results of this case study at the final time T. In particular, we display the free surface and the phase interface evolution (top panels) together with the phase velocities trend (bottom panels). The results provided by the TG2-PC method without and with the predictor/corrector strategy are displayed in the left and in the right column, respectively. It is evident how the predictor/correct step is able to suppress any spurious numerical oscillation due to the loss of hyperbolicity.

In a second analysis, we consider the presence of the excess pwp. We aim at numerically verify that Proposition 2.1 provides a sufficient condition to guarantee the hyperbolicity constraint in the case of a non-null excess pwp. For the excess pwp equation, we consider $C_v = 0.1$ m^2/s, $E_m = 0$ Pa and we assume an impermeable bottom so to prescribe a null flux at the bottom topography. Referring to Proposition 2.1, we observe that, also for this configuration, the hyperbolicity constraint is initially violated. Indeed, the initial value of the mean excess pwp and the initial flow conditions are such that $c_2 \approx a\beta$ and $c_1 \approx a$, thus resulting in an initial loss of hyperbolicity as $2c_2 < |v_{w,x} - v_{s,x}| < 2c_1$. In Fig. 3 we provide the trend of the free surface, the phase interface, the phase velocities and the isolines of the excess pwp at final time T. As for the previous setting, we compare the results yielded by the TG2-PC method when equipped, or not, with the predictor/corrector strategy used to enforce the hyperbolic regime. Analogously as in Fig. 2, we appreciate the capability of the predictor/corrector correction in removing spurious numerical oscillations due to the presence of complex eigenvalues.

4.1.3. Dam break over a flat plane

The first case study we reproduce was proposed in [40], where the authors employ a second-order total variation diminishing (TVD) FV scheme, and then reproduced successfully dealing with different numerical schemes [20,60]. Here, to assess the numerical performance of the proposed method, we build a reference solution following [20]. In particular, using a digitizer software [67], we extract data from a second-order space-time accurate TVD FV solution proposed in [40].

We consider a standard one-dimensional frictionless Riemann problem with infinite permeability, i.e. we assign $V_T = 10^{10}$ m/s. We

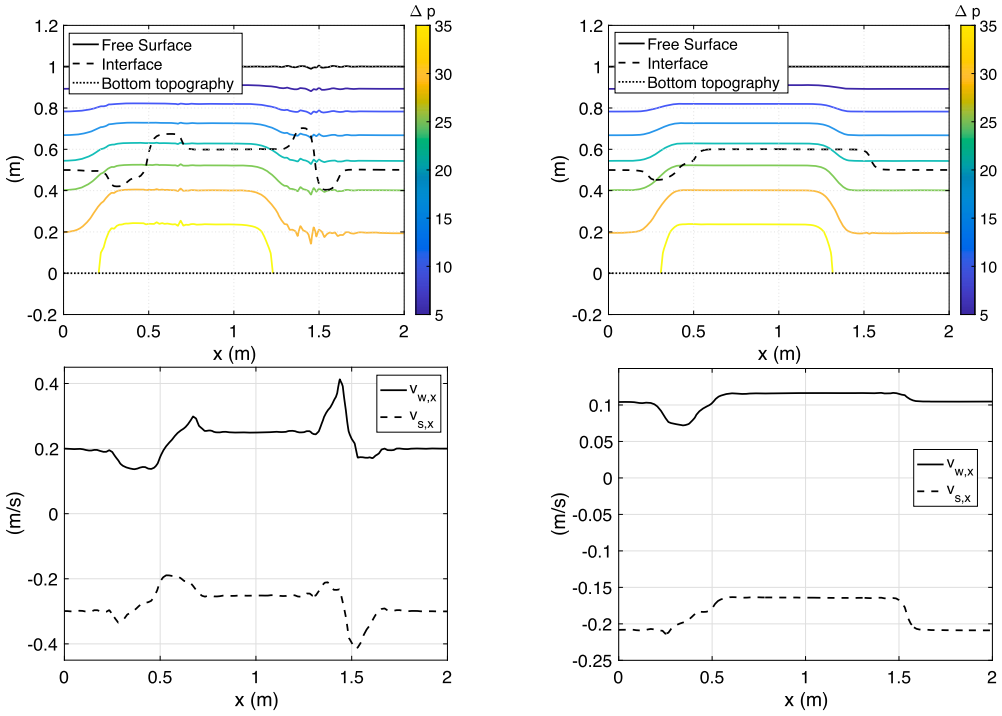

Fig. 3. Loss of hyperbolicity tests (non null excess pwp). Trend of the free surface, the phase interface and of the isolines of the excess pwp (top), and of the phase velocities (bottom) at final time T provided by the TG2-PC scheme without (left) and with (right) the predictor/corrector step. (For interpretation of the colors in the figure(s), the reader is referred to the web version of this article.)

take a flat square domain with edge length $L_x = L_y = 10$ m, a null excess pwp, a fluid at rest along the y-direction, a density ratio $r = 0.5$, and we neglect any erosion phenomenon. The initial conditions consist of two constant states, separated by an interface located at $x = L_x/2$, i.e.,

$$\mathbf{q}(\mathbf{x},0) = \begin{cases} (0.9, 2.1, 0.27, 0, -2.94, 0, 0)^T & \text{if } x < L_x/2, \\ (1.2, 0.8, -0.12, 0, -0.72, 0, 0)^T & \text{otherwise.} \end{cases} \tag{42}$$

Fig. 4 collects some results at time $T = 0.5$ s when performing the discretization on a fixed and on an adaptive grid. We provide the trend of the physical quantities h, h_w, h_s (panel a)); the phase velocities $v_{s,x}$, $v_{w,x}$ along the x-direction (panel b)); the solid volume fraction n_s (panel c)); the isolines of $U_{s,x}$ for the adaptive mesh case and the horizontal section used to extract the one-dimensional solutions in panels a)-c) (panel d)). In particular, the dashed lines and the lines with circles correspond to two different resolutions along the x-direction, namely a uniform spatial discretization $\Delta x \approx 0.16$ m (or, likewise, 2^{12} elements) for the dashed lines, and an adaptive discretization with a minimum resolution $\Delta x \approx 0.01$ m for the lines with circles. The mesh adaptation procedure is carried out at each time step of the simulation and is constrained by a minimum step length equal to the uniform mesh size adopted in [40]. The TG2-PC method, thanks to the PC strategy, is able to detect all the four waves generated by the Riemann problem. Moreover it is evident the excellent matching between reference and TG2-PC solution when resorting to the adapted mesh.

In a second test, we consider a wet-dry dam-break setting over a flat squared domain with extension along the two directions equal to $L = L_x = L_y = 100$ m and with densities $\rho = 2260$ kg/m^3, $\rho_w = 1000$ kg/m^3, $\rho_s = 2800$ kg/m^3, thus resulting in an initial liquid porosity $n_w = 0.3$. We consider a material initially at rest, and we set an initial material profile h equal to 10 m for $|x - L/2| \leq L/10$ and for $|y - L/2| \leq L/10$ and equal to 0 m otherwise. Concerning the bed friction, we do not consider any turbulence coefficient ξ, while we set a friction angle $\phi_B = 21.8°$. Then, we select a final time velocity $V_T = 10^{-3}$ m/s for the inter-phase drag force.
The spatial discretization is carried out by introducing a quadtree domain partition with a minimum mesh size equal to 1 m in the wet region and to 0.5 m along the wet-dry interface. Then, a mesh adaptation procedure is applied each 10^{-3} s.
We present the results obtained both by including and neglecting the excess pwp. Regarding the consolidation equation, we do not consider any odometric coefficient, namely $E_m = 0$ Pa, and we assign a consolidation coefficient $C_v = 0.01$ m^2/s. The final time is set to $T = 2.5$ s. Moreover, the initial condition varies linearly from the liquefied value at the bottom to the zero value at the top.
Fig. 5 displays some results of such an analysis. Panel a) shows the isolines of the mixture height h overlapped to the quadtree mesh at time $t = 1$ s, together with the white-highlighted horizontal line along which we extract the solution at the final time in case of a non-null (see panel b)) and a null (see panel c)) excess pwp. We observe that the presence of the excess pwp implies a larger runout. This is in accordance with the expectation, since, as already stated in the introduction, a possible mitigation strategy to slow down

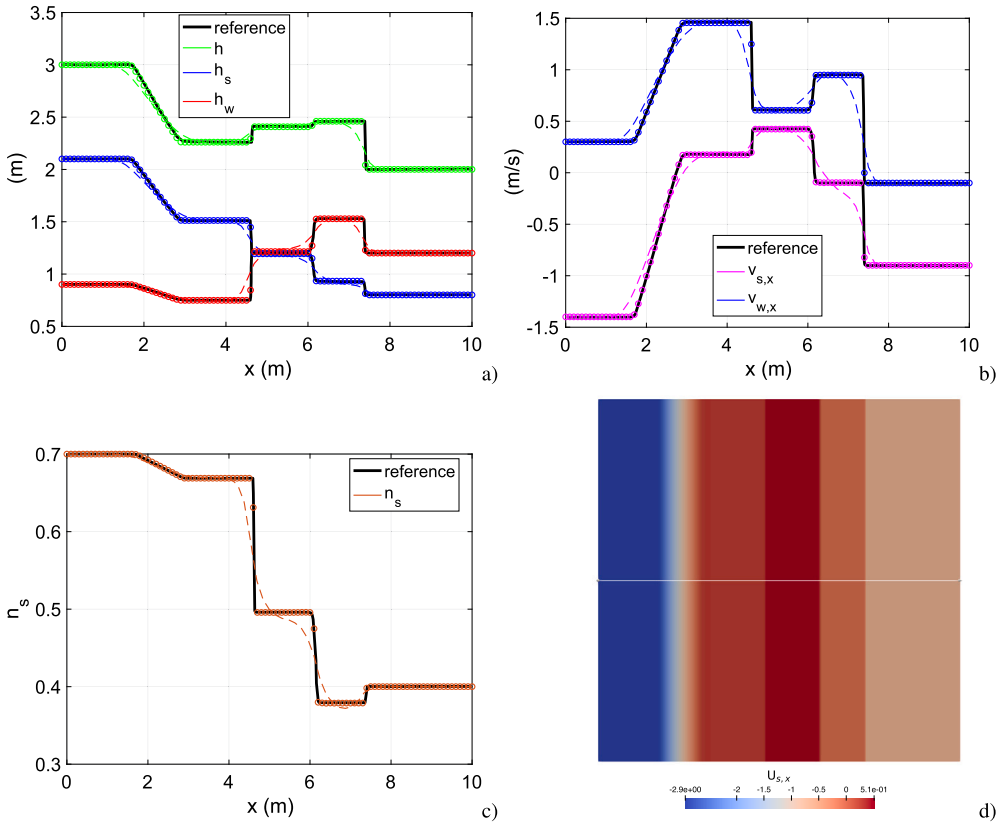

Fig. 4. Dam break problem over a flat bottom. Standard one-dimensional Riemann problem: trend of the total depth and of the fluid and solid landslide heights (panel a)); of the phase velocities along the x-direction (panel b)); of the solid volume fraction (panel c)) for two different spatial resolutions: one structured with $\Delta x \approx 0.16$ m, dashed lines; and one adaptive with finest resolution $\Delta x \approx 0.01$ m, lines with circles. Panel d) shows the isolines of $U_{s,x}$ for the adaptive mesh case together with the line over which we extract the one-dimensional solution displayed in the previous panels. (For interpretation of the colors in the figure(s), the reader is referred to the web version of this article.)

the landslide motion is the adoption of basal grids where the pore pressure is made zero. Moreover, panel b) shows that the isolines of the excess pwp relative to the liquefied state $\Delta p_{rel} = \frac{\Delta p}{\rho_d' g h}$ at the final time, such that $\Delta p_{rel} = 1$ in the liquefied state.

As a third test we consider a one-dimensional wet-dry dam-break problem over a flat bottom having extension $L = L_x = L_y = 100$ m, with densities $\rho = 2260$ kg/m^3, $\rho_w = 1000$ kg/m^3, $\rho_s = 2800$ kg/m^3, thus resulting in an initial liquid porosity $n_w = 0.3$. The material is initially at rest, and we set an initial material profile h equal to 10 m for $x \leq 10$ m and equal to 0 m otherwise. We consider a mild permeable condition, i.e., we assign $V_T = 10^{-3}$ m/s and a null excess pwp. Further, we neglect any erosion phenomenon. Concerning the bed friction, we do not consider any turbulence coefficient ξ, while we assign a null bed friction angle for a first set of simulations and a value $\phi_B = 21.8°$ for a second bunch of tests. For both the friction and frictionless case, we consider four different thresholds on the material and phase heights, i.e., 10^{-5} m, 10^{-4} m, 10^{-3} m, 10^{-2} m. Finally, we choose $T = 5$ s.
The domain is discretized with a structured grid having a resolution equal to $\Delta x \approx 0.4$ m. Fig. 6 gathers the results of such an analysis by considering the solution trend along the line $y = L/2$. In particular, panel a) shows the evolution of the solid front, i.e., $\max_{x \in [0,L]} h_s > 10^{-3}$, during the simulation time for the friction and frictionless cases and for the different thresholds. Panel b) shows a particular of the profile of the material height h close to the wet-dry interface. The arrows are associated with a reduction of the thresholds. We notice that a coarsening of the material threshold implies a lower simulated runout distance. In both the panels, it is evident a convergent trend of the solution for smaller and smaller values of the threshold.

4.1.4. Efficiency test with discontinuous topography

To test the parallel efficiency of the proposed numerical scheme, we perform a strong scaling analysis. Further, we show how such a scheme can handle the presence of discontinuities along the material path thanks to the adoption of the PC strategy.
To this aim, we choose a domain Ω with an extension along the x- and the y-direction equal to $L_x = L_y = 200$ m and a material with densities $\rho = 2260$ kg/m^3, $\rho_w = 1000$ kg/m^3, $\rho_s = 2800$ kg/m^3. No erosion effect is taken into account. Moreover, we consider no friction term ($\boldsymbol{\tau}_B^{(s)} = \mathbf{0}$), a terminal velocity $V_T = 10^{-3}$ m/s, a consolidation coefficient $C_v = 0.01$ m^2/s and a null odometric coefficient ($E_m = 0$ Pa). We assume both phases initially at rest and an topography profile with a discontinuity, being

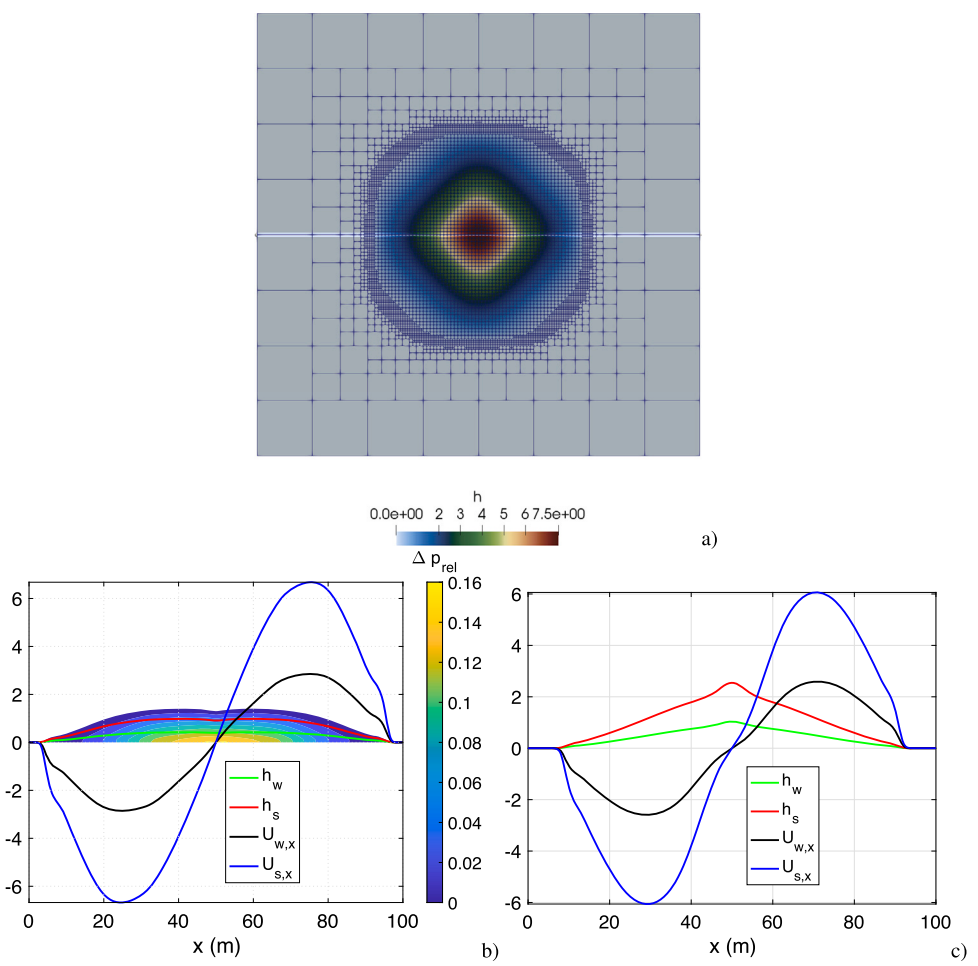

Fig. 5. Dam break problem over a flat bottom. Wet-dry dam-break problem: isolines of the mixture height h together with the quadtree mesh at $t = 1$ s (panel a)); trend of the fluid h_w and solid h_s landslide heights and of the horizontal fluid $U_{w,x}$ and solid $U_{s,x}$ mass fluxes for a non-null (panel b)) and a null (panel c)) excess pwp along the horizontal line white-highlighted in panel a). (For interpretation of the colors in the figure(s), the reader is referred to the web version of this article.)

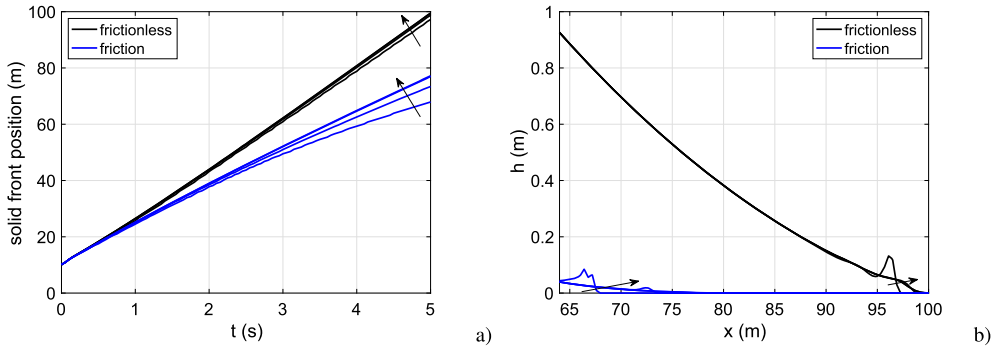

Fig. 6. Dam break problem over a flat bottom. One-dimensional wet-dry dam-break problem: time evolution of the solid front position (panel a)); trend of the material height h for a confined subset of the x coordinate (panel b)). Both the friction and frictionless scenarios are considered for different values of the thresholds (the arrows highlight the decreasing values of such quantities). (For interpretation of the colors in the figure(s), the reader is referred to the web version of this article.)

$$Z(\mathbf{x}) = \begin{cases} 95 & \text{if } x \leq 5, \\ -x + 100 & \text{if } 5 < x < 50, \\ 80 & \text{if } 60 < x < 100 \text{ and } 80 < y < 120, \\ 50 & \text{otherwise.} \end{cases} \tag{43}$$

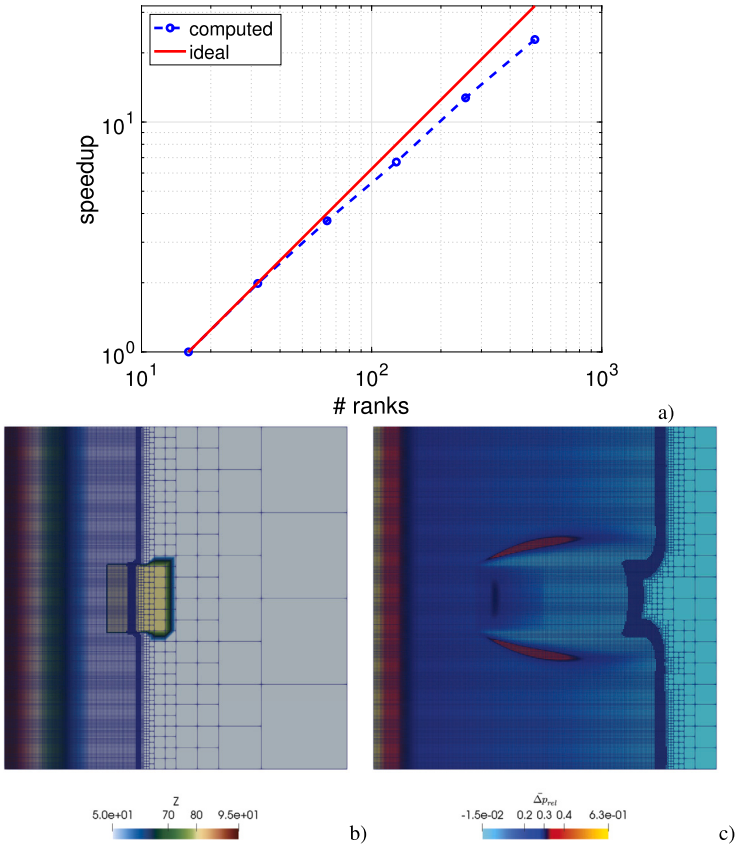

Fig. 7. Efficiency test. Scaling analysis (panel a)); isolines of the topography overlapped to the spatial discretization of the domain (panel b)); distribution of the relative mean excess pwp with respect to the mean liquefied value (panel c)).

The material height is initially set to 10 m, for $x \leq 10$ m, while the initial condition for the pressure is linearly varying from the liquefied value at the bottom to the null value at the free surface. Finally, the domain is discretized with a fixed uniform mesh characterized by a spatial resolution approximately equal to 0.2 m in both the directions, corresponding to a number of mesh elements equal to 2^{20}.

We carry out a strong scaling analysis, from 16 to 512 MPI ranks, and up to one second. Panel a) in Fig. 7 shows the speedup trend as a function of the number of ranks in a `log10-log10` scale. A parallel efficiency of roughly 70% is reached, with an increment close to the ideal one.

The same simulation has been replicated up to five seconds, and by resorting to a mesh adaptation procedure each 0.001 s. We set a minimum spatial resolution equal to 1 m in the wet region and to 0.5 m along the wet-dry interface. In particular, we show how the proposed method can handle discontinuities along the flow path, such as, for instance, in presence of houses.

In panel b) of Fig. 7 we supply the isolines of the topography discretized at time 2.5 s. Notice that the topography is properly refined as the landslide propagates. The distribution of the relative mean excess pwp with respect to the mean liquefied value, $\overline{\Delta p_{rel}}$, is shown in panel c) at the final time $t = 5$ s. The wake behind the parallelepipedal obstacle is characterized by a negative mean excess pwp, thus resulting in a low pressure area. This is in accordance with the expectation, the parallelepiped being a bluff obstacle. Moreover, even if the mean excess pwp is negative in the correspondence of the wake, the predictor/corrector penalization method allows keeping values in the hyperbolic range thus avoiding the rise of complex roots in the computation of the stabilization term for the momentum balance equation.

4.2. Sham Tseng San Tsuen debris flow

We focus on a real debris flow case study which has been already analyzed in the literature by using a Smoothed-Particle Hydrodynamics Finite-Difference (SPH-FD) scheme [3]. The event is a small sized debris flow which took place in Hong Kong on August 23, 1999. From geological surveys, it turns out that the landslide reached the village and destroyed a house, while it was estimated a material height ranging from 1 m to 1.5 m all over the village area (we refer to [3] for a detailed explanation of the study area).

The input topography is a Digital Terrain Model (DTM) with a resolution of 2 m in both the x- and the y-directions. We show the DTM isolines in Fig. 8, by highlighting the destroyed with a red dot.

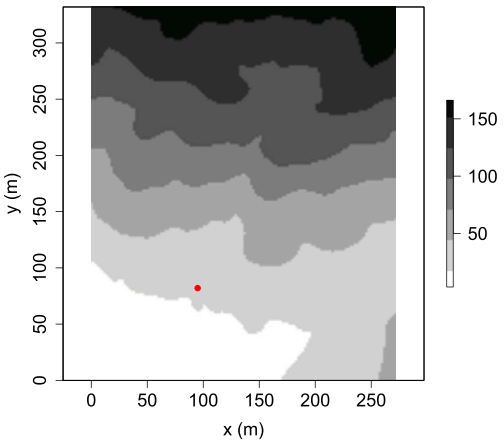

Fig. 8. Sham Tseng San Tsuen debris flow. DTM isolines with the destroyed house (red dot). (For interpretation of the colors in the figure(s), the reader is referred to the web version of this article.)

Regarding the parameters, we follow [3] and we choose: the bed friction angle ϕ_B such that $\tan\phi_B = 0.75$; the turbulence coefficient $\xi = 500$ m/s^2; the mixture and phase densities $\rho = 2000$ kg/m^3, $\rho_w = 1000$ kg/m^3, $\rho_s = 2400$ kg/m^3; the coefficients for the interphase drag law $V_T = 10^{-4}$ m/s, $m = 1$; the consolidation coefficient C_v such that we have a consolidation time $T_c = h_0^2/C_v = 78$ s for $h_0 = 1.5$ m; the odometric coefficient $E_m = 10^4$ Pa; the mixture material and phases height thresholds equal to 10^{-3} m.

We present results both with and without the consolidation equation, as in [3]. In particular, Fig. 9 shows the isolines of the material height from a minimum value of 10 cm superimposed to the DTM isolines at six different times ($t = 0$ s, 10 s, 20 s, 30 s, 45 s) for the case of a null excess pwp, while Fig. 10 provides the same results when including the excess pwp equation. We observe that the runout distance is considerably larger when including the excess pwp so that, in such a case, the landslide reaches the house that was destroyed during the real event. This is compliant with what obtained in [3]. Another similarity with respect to the SPH-FD code is the discrepancy between the case with and without excess pwp in terms of material height. By neglecting the excess pwp material height, deposit on the track is over 2 m. On the contrary, when including the excess pwp, we have material heights, ranging between 1 m and 1.2 m (i.e., in the range given by geological surveys), in the village area close to the destroyed house.

We experienced that the TG2-PC scheme predicts a lower front propagation runout when compared with the SPH-FD method. In more detail, we estimate a runout distance of about 233 m and 160 m for the case with and without excess pwp, respectively in contrast to approximately 270 m and 170 m for the SPH-FD code. This different behavior can be ascribed to the fact that the SPH discretization is, in general, overdiffusive, especially in advection dominated problems.

5. Conclusions

We have proposed a parallel efficient well-balanced numerical method to solve a two-phase depth-integrated consolidation mathematical model that has been originally proposed by M. Pastor in [3,24,25,4]. Such a model offers an extension of the Pitman-Le equations, to study the runout phase of fast landslides. In particular, we have proposed an extension of the Pelanti's proposition to consider the presence of non-null excess pwp.

The new scheme is second-order accurate in space and time and is subject to a stability restriction, which depends only on the horizontal CFL condition deriving from the mass and momentum equations. To this aim, a particular care has been taken to discretize the three-dimensional consolidation equation, by combining a semi-Lagrangian finite-difference approximation along the vertical direction, to model the free-surface varying a time, with a TG2-PC discretization in the horizontal domain.

We have tested the proposed numerical discretization on idealized as well as on realistic DTM scenarios. In particular, we have numerically verified the well-balancing property, the parallel efficiency and the capability to deal with discontinuous topographies. These positive checks candidate the proposed scheme as a valid alternative to other discretizations available in the literature, such as the SPH method. For instance, this latter could suffer from well-balancing issues and from an excessive dissipation when dealing with discontinuous topographies, such as in the presence of houses along the runout path.

Possible future developments include exploiting the parallel efficiency of the new method to apply an uncertainty quantification analysis to real case studies, for instance, by means of Monte Carlo sampling or polynomial chaos expansion [68–70].

CRediT authorship contribution statement

Federico Gatti: Conceptualization, Data curation, Formal analysis, Investigation, Methodology, Software, Validation, Visualization, Writing – original draft, Writing – review & editing. **Carlo de Falco:** Supervision, Writing – original draft, Writing – review & editing. **Simona Perotto:** Writing – original draft, Writing – review & editing. **Luca Formaggia:** Funding acquisition, Supervision. **Manuel Pastor:** Supervision.

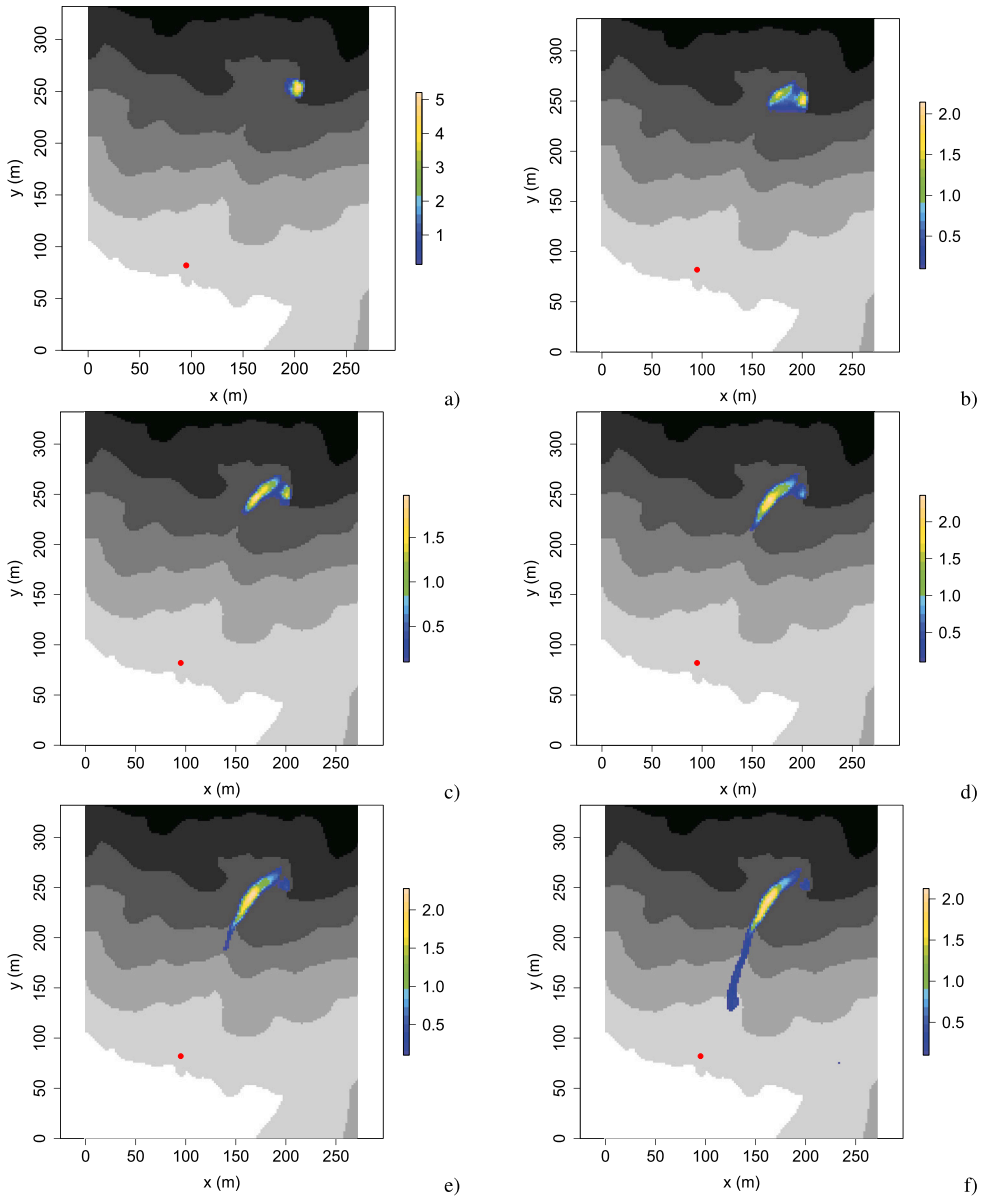

Fig. 9. Sham Tseng San Tsuen debris flow (null excess pwp). Isolines of the material height overlapped to the DTM isolines at time $t = 0$ s, 10 s, 20 s, 30 s, 45 s (from a) to f) panels). The red dot highlights the destroyed house. (For interpretation of the colors in the figure(s), the reader is referred to the web version of this article.)

Declaration of competing interest

The authors declare that they have no known competing financial interests or personal relationships that could have appeared to influence the work reported in this paper.

Data availability

Data will be made available on request.

Acknowledgements

This research was supported by the Accordo Attuativo ASI-POLIMI “Attività di Ricerca e Innovazione” n. 2018-5-HH.0. Partially funded by the European Union - NextGenerationEU and by the Ministry of University and Research (MUR), National Recovery and Resilience Plan (NRRP), Mission 4, Component 2, Investment 1.5, project “RAISE - Robotics and AI for Socio-economic Empowerment” (ECS00000035). F.G. is part of RAISE Innovation Ecosystem.

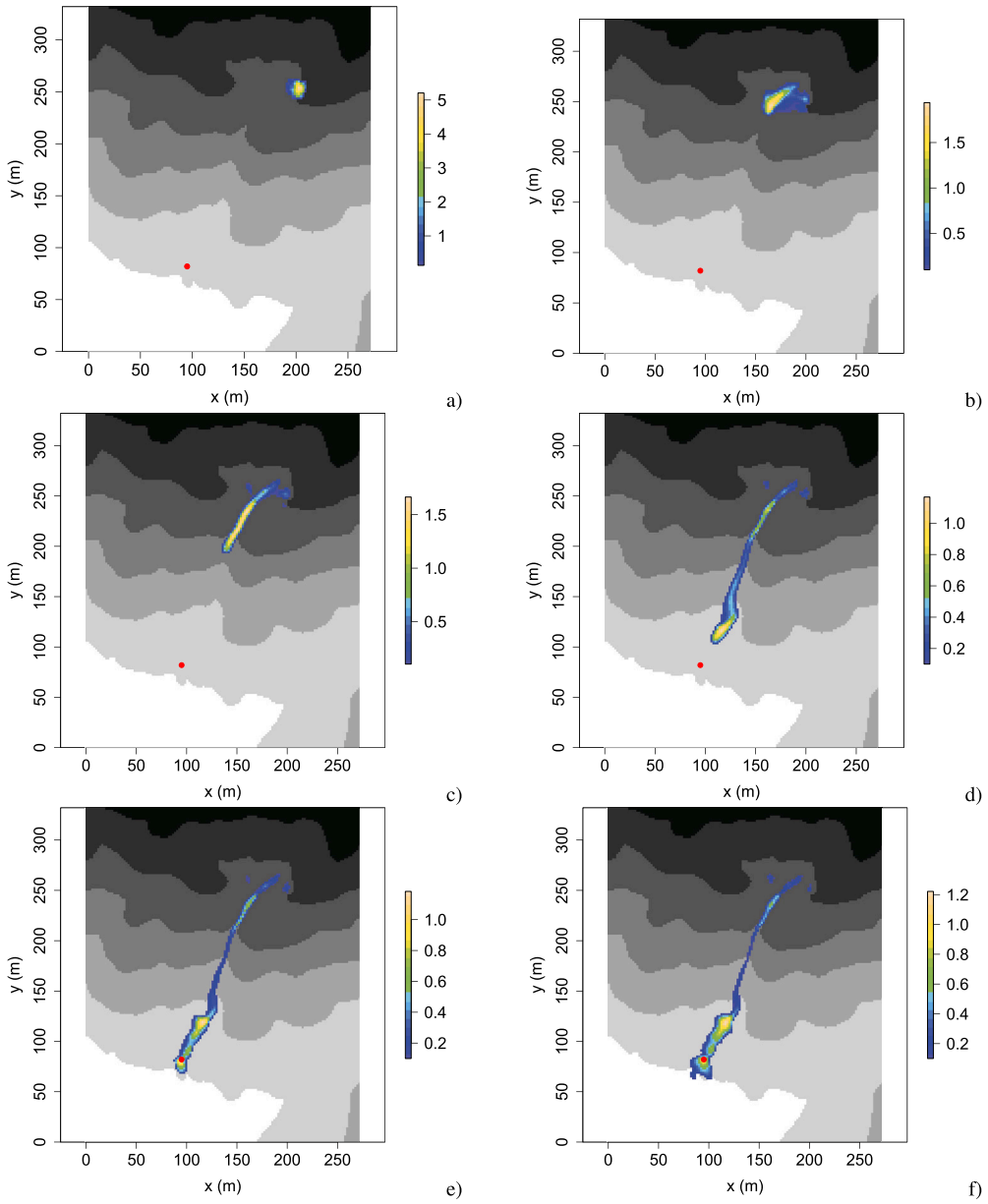

Fig. 10. Sham Tseng San Tsuen debris flow (non null excess pwp). Isolines of the material height overlapped to the DTM isolines at time $t = 0$ s, 10 s, 20 s, 30s, 45 s (from a) to f) panels). The red dot highlights the destroyed house. Isolines of the material height over the isolines of the DTM. The red dot is the house destroyed during the event. (For interpretation of the colors in the figure(s), the reader is referred to the web version of this article.)

C.d.F. and L.F. have been partially funded by the Italian Research Center on High-Performance Computing, Big Data and Quantum Computing (ICSC), European Union - Next Generation EU.

S.P. developed part of this research under the INdAM-GNCS2022 Project “Metodi di Riduzione Computazionale per le Scienze Applicate: Focus su Sistemi Complessi”.

The present research is within the framework of the project “Dipartimento di Eccellenza 2023-2027” granted by Italian MUR.

Finally, we thank Dr. Saeid M. Tayyebi for providing the initial material height and topography profile for the real test case scenario.

Appendix A. Proof of Proposition 2.1

We generalize the proof in [41, Proposition 4.1] to the case of a non-null excess pwp.
We consider the one-dimensional and homogeneous counterpart of the mass and momentum equations in (17), which simplifies to the semilinear equation

$$\partial_t \mathbf{q} + \mathbf{A}\partial_x \mathbf{q} = \mathbf{0}, \tag{A.1}$$

with $\mathbf{q} = (h_s, U_s, h_w, U_w)^T$ and $\mathbf{A} = \mathbf{A}(\mathbf{q})$ defined by

$$\begin{bmatrix} 0 & 1 & 0 & 0 \\ -\frac{n_w\overline{\Delta p}}{\rho_s} + \frac{1}{2}g(1-r)h_w + gh_s - v_s^2 & 2v_s & \frac{1}{2}g(1+r)h_s - \frac{n_w\overline{\Delta p}}{\rho_s} & 0 \\ 0 & 0 & 0 & 1 \\ \frac{n_w\overline{\Delta p}}{\rho_w} + gh_w & 0 & \frac{n_w\overline{\Delta p}}{\rho_w} + gh_w - v_w^2 & 2v_w \end{bmatrix}. \tag{A.2}$$

To simplify the notation, we neglect the subscript x for the mass fluxes, U_w, U_s, and the corresponding velocities, $v_w = U_w/h_w$, $v_s = U_s/h_s$. Moreover, we refer to an topography which does not vary in time, i.e., such that $\partial_t Z = 0$. This choice allows us to decrease by one the order of the system balance in (17).

As for the Pitman-Le equations, we recover a closed expression of the eigenvalues associated with the matrix $\mathbf{A}$ when imposing equal solid and liquid phase velocities ($v_w = v_s$). This allows us to identify the external (c_1) and the internal (c_2) wave celerities, and to introduce the quartic polynomials

$$\begin{aligned} p_w(\lambda) &= (\lambda - (v_s - c_2))(\lambda - (v_s + c_2))(\lambda - (v_w - c_1))(\lambda - (v_w + c_1)), \\ p_s(\lambda) &= (\lambda - (v_s - c_1))(\lambda - (v_s + c_1))(\lambda - (v_w - c_2))(\lambda - (v_w + c_2)). \end{aligned} \tag{A.3}$$

Note that the eigenvalues of $p_w(\lambda)$, $p_s(\lambda)$ are real numbers if and only if the following conditions hold,

$$\begin{cases} C \geq 0, \\ B \geq 0, \\ B^2 \geq C, \end{cases} \tag{A.4}$$

B and C being defined as in (12), which imply that

$$\begin{cases} C \geq 0, \\ \overline{\Delta p} \geq -\rho_w a^2 \left(\frac{1+\beta^2}{2\beta^2}\right), \\ \overline{\Delta p} \geq -\rho_w a^2. \end{cases} \tag{A.5}$$

Since the third condition is more restrictive than the second one and $C = B^2 \geq 0$ in case $\overline{\Delta p} = -\rho_w a^2$, we can conclude that the necessary and sufficient condition such that the eigenvalues of $p_w(\lambda)$, $p_s(\lambda)$ are real is

$$\overline{\Delta p} \geq -\rho_w a^2, \tag{A.6}$$

namely the left inequality in (14). Now, after denoting by $P = P(\lambda)$ the characteristic polynomial associated with the matrix $\mathbf{A}$, we can define the differences

$$P(\lambda) - p_w(\lambda) = \frac{1}{2\rho_w}(D - \sqrt{C})(v_s - v_w)(\lambda - \overline{v}), \tag{A.7}$$

$$P(\lambda) - p_s(\lambda) = \frac{1}{2\rho_w}(D + \sqrt{C})(v_s - v_w)(\lambda - \overline{v}), \tag{A.8}$$

with $\overline{v} = (v_s + v_w)/2$ and

$$D = 2n_w\overline{\Delta p}(1+r) + a^2\rho_w((3+r)n_w - 2). \tag{A.9}$$

Thus, it follows that the value taken by the characteristic polynomial P at λ is always lower- and upper-bounded by the values taken by the quartic polynomials p_w, p_s in (A.3), for any $\lambda \in \mathbb{R}$, if $D^2 \leq C$, which is equivalent to the two-side inequality

$$-\rho_w a^2 \leq \overline{\Delta p} \leq \rho_w a^2 \frac{1+r}{2}\frac{h_s}{h_w}. \tag{A.10}$$

We recover condition (A.6) from the left inequality. The upper bound introduces a further constraint on the mean excess pwp, in particular on the allowed maximum value. Thus, result (A.10) proves the two-side inequality in (11).

Regarding the sufficient conditions for hyperbolicity, we have to ensure that point $\overline{v}$ has to be included between the two inflection points, ω_1 and ω_2, of P, which is equivalent to require that

$$\frac{2\overline{\Delta p}(1-r)n_w}{\rho_w} + a^2((1-r)n_w + 2) + (v_w - v_s)^2 \geq 0, \tag{A.11}$$

namely

$$(v_w - v_s)^2 \geq -\frac{2\overline{\Delta p}(1-r)n_w}{\rho_w} - a^2((1-r)n_w + 2). \tag{A.12}$$

Such constraint is always satisfied since the right-hand side is always negative if (A.6) holds. The sufficient condition for hyperbolicity (i.e., $P(\overline{v}) \geq 0$) enforces inequality

$$4\overline{\Delta p}(r-1)n_w\left(2a^2 - \Delta v^2\right) + \left(4a^2 - \Delta v^2\right)\left(2a^2(r-1)n_w + \Delta v^2\right) \leq 0, \tag{A.13}$$

with $\Delta v = (v_w - v_s)$, which leads to (13) when solved in terms of Δv. This concludes the proof.

Appendix B. Stability and local truncation error analysis of the TG2 scheme with explicit treatment of the diffusion term

For simplicity, we consider the one-dimensional linear problem

$$\partial_t q + a\partial_x q - \epsilon\partial_{xx} q = 0 \tag{B.1}$$

for the generic scalar variable q. We apply the TG2 method to discretize (B.1). This leads to

$$q_i^{n+1} = q_i^n - a\frac{\Delta t}{2\Delta x}\left(q_{i+1}^n - q_{i-1}^n\right) + a^2\frac{\Delta t^2}{2\Delta x^2}\left(q_{i+1}^n - 2q_i^n + q_{i-1}^n\right) + \epsilon\frac{\Delta t}{\Delta x^2}\left(q_{i+1}^n - 2q_i^n + q_{i-1}^n\right), \tag{B.2}$$

for each (spatial) node i and time t^n.
By introducing the adimensional coefficients $\mu = a\frac{\Delta t}{\Delta x}$ and $\Phi = \epsilon\frac{\Delta t}{\Delta x^2}$ and after applying the von Neumann analysis to (B.2), we obtain the amplification factor

$$G = (1 - \mu^2 - 2\Phi) + (\mu^2 + 2\Phi)\cos\vartheta - j\mu\sin\vartheta,$$

with j the imaginary unit and ϑ an angle in $[0, \pi]$. The stability condition $|G|^2 \leq 1$ for the most restrictive choice of ϑ, i.e., $\vartheta = \pi$, leads to inequality

$$\mu^2 + 2\Phi \leq 1,$$

namely to $\Phi \leq \frac{1}{2}$. The explicit definitions of μ and Φ imply that

$$\Delta t \leq \frac{\Delta x^2}{2\epsilon}(1 - \mu^2),$$

which coincides with result (34).

To prove the second order of convergence of the scheme (B.2), we compute the associated local truncation error moving from the Taylor series expansions

$$q_i^{n+1} = q_i^n + \Delta t\partial_t q_i^n + \frac{\Delta t^2}{2}\partial_{tt} q_i^n + \mathcal{O}(\Delta t^3),$$
$$q_{i+1}^n = q_i^n + \Delta x\partial_x q_i^n + \frac{\Delta x^2}{2}\partial_{xx} q_i^n + \frac{\Delta x^3}{6}\partial_{xxx} q_i^n + \mathcal{O}(\Delta x^4),$$
$$q_{i-1}^n = q_i^n - \Delta x\partial_x q_i^n + \frac{\Delta x^2}{2}\partial_{xx} q_i^n - \frac{\Delta x^3}{6}\partial_{xxx} q_i^n + \mathcal{O}(\Delta x^4),$$

after assuming enough regularity for q. Replacing such expansions in (B.2) yields

$$\partial_t q_i^n + \frac{\Delta t}{2}\partial_{tt} q_i^n + \mathcal{O}(\Delta t^2) = -a\partial_x q_i^n + a^2\frac{\Delta t}{2}\partial_{xx} q_i^n + \epsilon\partial_{xx} q_i^n + \mathcal{O}(\Delta x^2).$$

Since we have $\partial_t q_i^n + a\partial_x q_i^n - \epsilon\partial_{xx} q_i^n = 0$ and $\partial_{tt} q_i^n = a^2\partial_{xx} q_i^n - 2a\epsilon\partial_{xxx} q_i^n + \epsilon^2\partial_{xxxx} q_i^n$, it turns out that the local truncation error τ for (B.2) is given by

$$\tau = \frac{\Delta t}{2}\left(-2a\epsilon\partial_{xxx} q_i^n + \epsilon^2\partial_{xxxx} q_i^n\right) + \mathcal{O}(\Delta t^2 + \Delta x^2).$$

Thus, method (B.2) is second order accurate when the diffusion coefficient is at most equal to the time step size, i.e. for $\epsilon \sim \mathcal{O}(\Delta t)$. This is, for instance, normally verified by advection dominated problems.

References

[1] E.B. Pitman, L. Le, A two-fluid model for avalanche and debris flows, Philos. Trans. - Royal Soc., Math. Phys. Eng. Sci. 363 (2005) 1573–1601.
[2] S.P. Pudasaini, A general two-phase debris flow model, J. Geophys. Res., Earth Surf. 117 (2012).
[3] M. Pastor, S.M. Tayyebi, M.M. Stickle, Á. Yagüe, M. Molinos, P. Navas, D. Manzanal, A depth integrated, coupled, two-phase model for debris flow propagation, Acta Geotech. (2021) 1–25.
[4] M. Pastor, S.M. Tayyebi, M.M. Stickle, M. Molinos, A. Yague, D. Manzanal, P. Navas, An arbitrary Lagrangian Eulerian (ALE) finite difference (FD)-SPH depth integrated model for pore pressure evolution on landslides over erodible terrains, Int. J. Numer. Anal. Methods Geomech. 46 (2022) 1127–1153.
[5] A.L. Yifru, E. Laache, H. Norem, S. Nordal, V. Thakur, Laboratory investigation of performance of a screen type debris-flow countermeasure, Trans. Hong Kong Inst. Eng. 25 (2018) 129–144.

[6] L. Cascini, S. Cuomo, M. Pastor, I. Rendina, SPH-FDM propagation and pore water pressure modelling for debris flows in flume tests, Eng. Geol. 213 (2016) 74–83.
[7] Y. Gonda, Function of a debris-flow brake, Int. J. Erosion Control Eng. 2 (2009) 15–21.
[8] F. Gatti, C. de Falco, S. Perotto, L. Formaggia, A scalable well-balanced numerical scheme for the simulation of fast landslides with efficient time stepping, Appl. Math. Comput. 468 (2024) 128525.
[9] M. Quecedo, M. Pastor, A reappraisal of Taylor–Galerkin algorithm for drying–wetting areas in shallow water computations, Int. J. Numer. Methods Fluids 38 (2002) 515–531.
[10] M. Quecedo, M. Pastor, M.I. Herreros, J.A. Fernández Merodo, Numerical modelling of the propagation of fast landslides using the finite element method, Int. J. Numer. Methods Eng. 59 (2004) 755–794.
[11] F. Gatti, M. Fois, C. de Falco, S. Perotto, L. Formaggia, Parallel simulations for fast-moving landslides: space-time mesh adaptation and sharp tracking of the wetting front, Int. J. Numer. Methods Fluids 95 (2023) 1286–1309.
[12] C. Parés, Numerical methods for nonconservative hyperbolic systems: a theoretical framework, SIAM J. Numer. Anal. 44 (2006) 300–321.
[13] M.J. Castro, E.D. Fernández-Nieto, A.M. Ferreiro, J.A. García-Rodríguez, C. Parés, High order extensions of Roe schemes for two-dimensional nonconservative hyperbolic systems, J. Sci. Comput. 39 (2009) 67–114.
[14] M. Castro, J.M. Gallardo, J.A. López-GarcÍa, C. Parés, Well-balanced high order extensions of Godunov's method for semilinear balance laws, SIAM J. Numer. Anal. 46 (2008) 1012–1039.
[15] J.M. Gallardo, C. Parés, M. Castro, On a well-balanced high-order finite volume scheme for shallow water equations with topography and dry areas, J. Comput. Phys. 227 (2007) 574–601.
[16] M. Dumbser, E.F. Toro, A simple extension of the Osher Riemann solver to non-conservative hyperbolic systems, J. Sci. Comput. 48 (2011) 70–88.
[17] S. Busto, M. Dumbser, S. Gavrilyuk, K. Ivanova, On thermodynamically compatible finite volume methods and path-conservative ADER discontinuous Galerkin schemes for turbulent shallow water flows, J. Sci. Comput. 88 (2021) 28.
[18] M. Castro, J. Gallardo, C. Parés, High order finite volume schemes based on reconstruction of states for solving hyperbolic systems with nonconservative products. Applications to shallow-water systems, Math. Comput. 75 (2006) 1103–1134.
[19] S. Rhebergen, O. Bokhove, J. van der Vegt, Discontinuous Galerkin finite element methods for hyperbolic nonconservative partial differential equations, J. Comput. Phys. 227 (2008) 1887–1922.
[20] M. Dumbser, M. Castro, C. Parés, E.F. Toro, ADER schemes on unstructured meshes for nonconservative hyperbolic systems: applications to geophysical flows, Comput. Fluids 38 (2009) 1731–1748.
[21] S. Busto, M. Dumbser, A staggered semi-implicit hybrid finite volume / finite element scheme for the shallow water equations at all Froude numbers, Appl. Numer. Math. 175 (2022) 108–132.
[22] F. Gatti, L. Bonaventura, A. Menafoglio, M. Papini, L. Longoni, A fully coupled superficial runoff and soil erosion basin scale model with efficient time stepping, Comput. Geosci. 177 (2023) 105362.
[23] M. Pastor, B. Haddad, G. Sorbino, S. Cuomo, V. Drempetic, A depth-integrated, coupled SPH model for flow-like landslides and related phenomena, Int. J. Numer. Anal. Methods Geomech. 33 (2009) 143–172.
[24] M. Pastor, A. Yague, M. Stickle, D. Manzanal, P. Mira, A two-phase SPH model for debris flow propagation, Int. J. Numer. Anal. Methods Geomech. 42 (2018) 418–448.
[25] M. Pastor, T. Blanc, B. Haddad, S. Petrone, M. Sanchez Morles, V. Drempetic, D. Issler, G. Crosta, L. Cascini, G. Sorbino, et al., Application of a SPH depth-integrated model to landslide run-out analysis, Landslides 11 (2014) 793–812.
[26] X. Xia, Q. Liang, M. Pastor, W. Zou, Y.-F. Zhuang, Balancing the source terms in a SPH model for solving the shallow water equations, Adv. Water Resour. 59 (2013) 25–38.
[27] S. Soares-Frazão, J. Lhomme, V. Guinot, Y. Zech, Two-dimensional shallow-water model with porosity for urban flood modelling, J. Hydraul. Res. 46 (2008) 45–64.
[28] V. Guinot, C. Delenne, Macroscopic modelling of urban floods, Houille Blanche (2014) 19–25.
[29] Y. Fan, T. Ao, H. Yu, G. Huang, X. Li, A coupled 1D-2D hydrodynamic model for urban flood inundation, Adv. Meteorol. (2017) 2017.
[30] P.J. Pritchard, R.W. Fox, A.T. McDonald, Introduction to Fluid Mechanics, John Wiley & Sons, 2010.
[31] K. Hutter, Y. Wang, S.P. Pudasaini, The Savage–Hutter avalanche model: how far can it be pushed?, Philos. Trans. - Royal Soc., Math. Phys. Eng. Sci. 363 (2005) 1507–1528.
[32] R.M. Iverson, The physics of debris flows, Rev. Geophys. 35 (1997) 245–296.
[33] S.G. Evans, O. Hungr, J.J. Clague, Dynamics of the 1984 rock avalanche and associated distal debris flow on Mount Cayley, British, Columbia, Canada; Implications for landslide hazard assessment on dissected volcanoes, Eng. Geol. 61 (2001) 29–51.
[34] R. Sosio, G.B. Crosta, O. Hungr, Complete dynamic modeling calibration for the Thurwieser rock avalanche (Italian Central Alps), Eng. Geol. 100 (2008) 11–26.
[35] P. Bartelt, Y. Bühler, O. Buser, M. Christen, L. Meier, Modeling mass-dependent flow regime transitions to predict the stopping and depositional behavior of snow avalanches, J. Geophys. Res., Earth Surf. 117 (2012).
[36] T.B. Anderson, R. Jackson, Fluid mechanical description of fluidized beds. Equations of motion, Ind. Eng. Chem. Fundam. 6 (1967) 527–539.
[37] S.M. Tayyebi, M. Pastor, A. Hernandez, L. Gao, M.M. Stickle, A.L. Yifru, V. Thakur, Two-phase two-layer depth-integrated SPH-FD model: application to lahars and debris flows, Land 11 (2022) 1629.
[38] S.M. Tayyebi, M. Pastor, M.M. Stickle, Á. Yagüe, D. Manzanal, M. Molinos, P. Navas, SPH numerical modelling of landslide movements as coupled two-phase flows with a new solution for the interaction term, Eur. J. Mech. B, Fluids 96 (2022) 1–14.
[39] M. Pastor, T. Blanc, B. Haddad, V. Drempetic, M.S. Morles, P. Dutto, M.M. Stickle, P. Mira, J.F. Merodo, Depth averaged models for fast landslide propagation: mathematical, rheological and numerical aspects, Arch. Comput. Methods Eng. 22 (2015) 67–104.
[40] M. Pelanti, F. Bouchut, A. Mangeney, A Roe-type scheme for two-phase shallow granular flows over variable topography, ESAIM: Math. Model. Numer. Anal. (Modélisation Mathématique et Analyse Numérique) 42 (2008) 851–885.
[41] M. Pelanti, F. Bouchut, A. Mangeney, A Riemann solver for single-phase and two-phase shallow flow models based on relaxation. Relations with Roe and VFRoe solvers, J. Comput. Phys. 230 (2011) 515–550.
[42] S. Qamar, S. Zia, W. Ashraf, The space–time CE/SE method for solving single and two-phase shallow flow models, Comput. Fluids 96 (2014) 136–151.
[43] J.M. Greenberg, A.-Y. LeRoux, A well-balanced scheme for the numerical processing of source terms in hyperbolic equations, SIAM J. Numer. Anal. 33 (1996) 1–16.
[44] R.J. LeVeque, Balancing source terms and flux gradients in high-resolution Godunov methods: the quasi-steady wave-propagation algorithm, J. Comput. Phys. 146 (1998) 346–365.
[45] K. Xu, A well-balanced gas-kinetic scheme for the shallow-water equations with source terms, J. Comput. Phys. 178 (2002) 533–562.
[46] M.E. Vázquez-Cendón, Improved treatment of source terms in upwind schemes for the shallow water equations in channels with irregular geometry, J. Comput. Phys. 148 (1999) 497–526.
[47] S. Noelle, N. Pankratz, G. Puppo, J.R. Natvig, Well-balanced finite volume schemes of arbitrary order of accuracy for shallow water flows, J. Comput. Phys. 213 (2006) 474–499.
[48] S. Noelle, Y. Xing, C.-W. Shu, High-order well-balanced finite volume weno schemes for shallow water equation with moving water, J. Comput. Phys. 226 (2007) 29–58.

[49] P. Garcia-Navarro, M.E. Vazquez-Cendon, On numerical treatment of the source terms in the shallow water equations, Comput. Fluids 29 (2000) 951–979.
[50] E. Audusse, F. Bouchut, M.-O. Bristeau, R. Klein, B.t. Perthame, A fast and stable well-balanced scheme with hydrostatic reconstruction for shallow water flows, SIAM J. Sci. Comput. 25 (2004) 2050–2065.
[51] O. Gourgue, R. Comblen, J. Lambrechts, T. Kärnä, V. Legat, E. Deleersnijder, A flux-limiting wetting–drying method for finite-element shallow-water models, with application to the Scheldt estuary, Adv. Water Resour. 32 (2009) 1726–1739.
[52] H. Liu, J. Zou, Some new additive Runge–Kutta methods and their applications, J. Comput. Appl. Math. 190 (2006) 74–98. Special Issue: International Conference on Mathematics and its Application.
[53] P.C. Africa, Scalable adaptive simulation of organic thin-film transistors, PhD Thesis in: Mathematical Models and Methods in Engineering, Politecnico di Milano, Milano, Italy, 2019.
[54] S.T. Zalesak, Fully multidimensional flux-corrected transport algorithms for fluids, J. Comput. Phys. 31 (1979) 335–362.
[55] J.P. Boris, D.L. Book, Flux-corrected transport. iii. Minimal-error FCT algorithms, J. Comput. Phys. 20 (1976) 397–431.
[56] D. Kuzmin, M. Möller, S. Turek, High-resolution FEM–FCT schemes for multidimensional conservation laws, Comput. Methods Appl. Mech. Eng. 193 (2004) 4915–4946.
[57] V. Casulli, Semi-implicit finite difference methods for the two-dimensional shallow water equations, J. Comput. Phys. 86 (1990) 56–74.
[58] V. Casulli, R.T. Cheng, Semi-implicit finite difference methods for three-dimensional shallow water flow, Int. J. Numer. Methods Fluids 15 (1992) 629–648.
[59] M.J. Castro-Díaz, E.D. Fernández-Nieto, J.M. González-Vida, C. Parés-Madroñal, Numerical treatment of the loss of hyperbolicity of the two-layer shallow-water system, J. Sci. Comput. 48 (2011) 16–40.
[60] J. Zhai, W. Liu, L. Yuan, Solving two-phase shallow granular flow equations with a well-balanced NOC scheme on multiple GPUs, Comput. Fluids 134–135 (2016) 90–110.
[61] M. Castro, A. Pardo, C. Parés, E. Toro, On some fast well-balanced first order solvers for nonconservative systems, Math. Comput. 79 (2010) 1427–1472.
[62] K. Boukir, Y. Maday, B. Métivet, A high order characteristics method for the incompressible Navier–Stokes equations, Comput. Methods Appl. Mech. Eng. 116 (1994) 211–218.
[63] K. Boukir, Y. Maday, B. Métivet, E. Razafindrakoto, A high-order characteristics/finite element method for the incompressible Navier-Stokes equations, Int. J. Numer. Methods Fluids 25 (1997) 1421–1454.
[64] I. Babuška, The finite element method with penalty, Math. Comput. 27 (1973) 221–228.
[65] L. Formaggia, F. Gatti, S. Zonca, An XFEM/DG approach for fluid-structure interaction problems with contact, Appl. Math. 66 (2021) 183–211.
[66] Y. Xing, C.-W. Shu, A new approach of high order well-balanced finite volume WENO schemes and discontinuous Galerkin methods for a class of hyperbolic systems with source terms, Comput. Phys. 1 (2006) 100–134.
[67] A. Rohatgi, Webplotdigitizer: Version 4.6, 2022.
[68] B. Sudret, Global sensitivity analysis using polynomial chaos expansions, Reliab. Eng. Syst. Saf. 93 (2008) 964–979.
[69] M.S. Bernardi, P.C. Africa, C. de Falco, L. Formaggia, A. Menafoglio, S. Vantini, On the use of interferometric synthetic aperture radar data for monitoring and forecasting natural hazards, Math. Geosci. (2021) 1–32.
[70] R. Schobi, B. Sudret, J. Wiart, Polynomial-chaos-based Kriging, Int. J. Uncertain. Quantificat. 5 (2015) 171–193.